ELSEVIER

Journal of the Mechanics and Physics of Solids
52 (2004) 941–974

JOURNAL OF THE
MECHANICS AND
PHYSICS OF SOLIDS

www.elsevier.com/locate/jmps

Onset of failure in finitely strained layered composites subjected to combined normal and shear loading

M.D. Nestorović, N. Triantafyllidis*

Department of Aerospace Engineering, The University of Michigan, Ann Arbor, MI 48109-2140, USA

Received 4 February 2003; received in revised form 16 June 2003; accepted 24 June 2003

Abstract

A limiting factor in the design of fiber-reinforced composites is their failure under axial compression along the fiber direction. These critical axial stresses are significantly reduced in the presence of shear stresses. This investigation is motivated by the desire to study the onset of failure in fiber-reinforced composites under arbitrary multi-axial loading and in the absence of the *experimentally inevitable* imperfections and finite boundaries.

By using a finite strain continuum mechanics formulation for the bifurcation (buckling) problem of a rate-independent, perfectly periodic (layered) solid of infinite extent, we are able to study the influence of load orientation, material properties and fiber volume fraction on the onset of instability in fiber-reinforced composites. Two applications of the general theory are presented in detail, one for a finitely strained elastic rubber composite and another for a graphite–epoxy composite, whose constitutive properties have been determined experimentally. For the latter case, extensive comparisons are made between the predictions of our general theory and the available experimental results as well as to the existing approximate structural theories. It is found that the load orientation, material properties and fiber volume fraction have substantial effects on the onset of failure stresses as well as on the type of the corresponding mode (local or global).

Keywords: A. Buckling; A. Microstructures; B. Finite strain; B. Layered material

* Corresponding author. Tel.: +1-734-763-2356; fax: +1-734-763-0578.
E-mail address: nick@engin.umich.edu (N. Triantafyllidis).

0022-5096/$ - see front matter © 2003 Elsevier Ltd. All rights reserved.
doi:10.1016/j.jmps.2003.06.001

1. Introduction and motivation

Fiber-reinforced polymer matrix composites have become widely used in engineering applications because of their high stiffness and strength-to-weight ratios when compared to the conventional structural materials. In spite of the significant improvements in properties like the impact resistance, energy absorption and tensile strength, the compressive strength of these composites is significantly less than their tensile strength. It was also observed that shear applied simultaneously with compression along the fiber direction further lowers the strength of these composites. This has reduced the advantageous position of these materials in spite of their long established and widespread use, and has stipulated further study of their mechanical properties, in particular the behavior of these materials under multi-axial loading conditions.

The importance of shear on the onset of instability of unidirectional fiber composites was first recognized in early works by Rosen (1965), who modeled fibers embedded in a matrix as elastic beams on an elastic foundation, in order to estimate the compressive stress at which the fibers buckle. In spite of all the extensions and improvements, the analysis for which the constituents are assumed to be elastic yields compressive strengths which are significantly higher than those measured in the experiments. It is now widely known that the compressive strains at failure of these composites are such that the matrix yields, and the first effort to account for this effect appeared in Schuerch (1966). Argon (1972) was the first to point out that the aligned fiber composites have small fiber misalignments and that under axial compression the matrix can develop local shear stresses. When these shear stresses reach the yield stress of the composite, the shear modulus decays, and this results in a maximum load type instability which further develops into a kink band. The sensitivity of the critical stress to fiber misalignments was reaffirmed by Budiansky (1983), who extended the work of Argon (1972) by considering the response of a zero angle kink band in unidirectional composites with elastoplastic shear response. A significant extension of this work is presented in Budiansky and Fleck (1993) to include the analysis of inclined kink bands and combined axial compression and shear loading.

Following the initial works of Argon (1972) and Budiansky (1983), there has been an abundance of approximate structural models which improved and extended these ideas on the stability of unidirectional fiber composites. Our purpose here is not to review this voluminous literature on the failure mechanics of fiber-reinforced composites. Of particular interest to the present work are the recent experimental and analytical studies in Kyriakides et al. (1995), on the failure of fiber-reinforced polymer matrix composites. These researchers modeled the composite as a two-dimensional solid with alternating layers representing the elastic fibers and inelastic matrix with an initial waviness. This work was further extended in Hsu et al. (1998), who modeled the same composite as a three-dimensional solid with circular elastic fibers which are hexagonally distributed inside an inelastic matrix, also with an initial waviness. In both works the properties of the constituents were selected so that the shear response of the model material matched that of the graphite–epoxy (AS4/PEEK) composite. Both models developed a limit load under axial compression, which was followed by localized bending in well-defined narrow bands across the specimen. It was observed that the fibers inside

the band bend and rotate in a similar fashion to the kink bands reported from the compressive failure experiments. Vogler et al. (2000) further extended both models to complement their experimental studies, by modeling failure under combined axial compression and shear loading.

The aforementioned experiments on composites and the corresponding numerical calculations model the deformation of the imperfect finite sized specimens from the stress-free state, through the initial maximum load and subsequent localization of deformation in narrow bands, all the way to complete collapse of the entire specimen. However, this work pertains only to certain loading orientations and boundary conditions, the ones which best describe their experimental setup. Important issues regarding the dependence of the mechanical properties of these materials on the macroscopic loading orientation and geometry without the influence of imperfections and boundary effects have not been addressed, partially due to the limitations of the experimental procedures.

It should also be mentioned at this point that the stability of layered media under multi-axial loading plays an important part in many engineering applications, besides the fiber-reinforced composites. Metal-reinforced rubbers, in the form of reinforced tires or composite pads (see Rivin, 1983), are some examples of these applications. On a smaller scale the same layered morphology appears as the salient microstructural feature in the glassy–rubbery copolymers, whose macroscopic behavior is closely linked to the instabilities associated with their layered microstructure (see Cohen et al., 2000). Clearly the stability of finitely strained layered elastomeric composites requires a large strain continuum mechanics formulation of the problem, an approach that was not necessary for the modeling of fiber-reinforced composites.

As the first step in the direction of using a continuum mechanics approach to model these types of problems, Triantafyllidis and Maker (1985) have studied the bifurcation problem of a finitely strained, rate-independent, fiber-reinforced composite of infinite extent under axial compression. It was found that the macroscopic (global) failure predictions, which correspond to the onset of first long-wavelength type instability, are an upper bound to the microscopic (local) failure predictions, which correspond to the onset of first bifurcation instability in the solid. Subsequent work by Geymonat et al. (1993) proposed a general theory to investigate the failure surfaces in periodic solids of infinite extent. It was shown that if the critical wavelength is much larger than the unit cell size, the first instability can also be determined from the macroscopic properties of the infinite medium as the first loss of ellipticity of the homogenized moduli of the periodic solid. The usefulness of these onset of failure surfaces is that they provide a consistent upper bound for the onset of failure in the corresponding actual composite materials with random imperfections (see Triantafyllidis and Schraad, 1998 for the case of aluminum honeycombs) and allow the possibility to investigate arbitrary macroscopic loading, which is exactly what is done in the present work.

The outline of this paper is as follows: In Section 2 the plane strain bifurcation problem is formulated for an infinite, perfectly periodic, rate-independent composite. Following a description of the macroscopic loading paths considered, the methodology for calculating the principal equilibrium solution is given next for two different

types of layered composites. The results of the analysis are presented and discussed in Section 3, for the following two composites: one is motivated by the microstructural instability mechanisms in copolymer films and metal-reinforced rubbers, and is made of two alternating layers of a compressible foam rubber and the other is made of graphite–epoxy, and whose properties have been determined experimentally by Vogler et al. (2000). The paper is concluded with the discussion of the above presented work and suggestions for further work in Section 4.

2. Problem formulation

In this section, the plane strain bifurcation problem for an infinite, perfectly periodic (layered), rate-independent solid is formulated. The goal is to find the critical loading corresponding to the first bifurcation of the layered medium as the loading parameter increases from zero, along a specified loading path. The section is divided into three parts. The governing equations and bifurcation analysis are presented first, followed by a description of the loading process in the second part. The choice of constitutive laws for finite elasticity and elastoplasticity is given in the last part.

2.1. Governing equations and bifurcation analysis

Consider an infinite, perfectly periodic solid composed of a self-repeating sequence of two layers, each made of a homogeneous, rate-independent material as depicted in Fig. 1. The two layers m (matrix) and f (fiber) have initial thicknesses H_m and H_f in the undeformed, stress-free configuration which is used as the reference configuration. The solid is deformed under finite plane strain conditions and perfect bonding between the layers is assumed, i.e., the tractions and displacements are continuous across each interface for all possible deformations. A full Lagrangian formulation of the problem

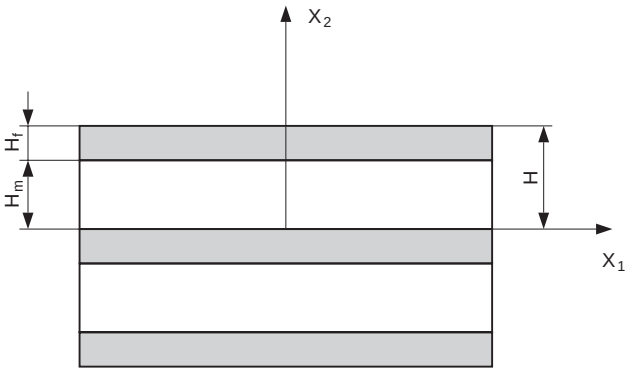

Fig. 1. Schematic representation of an infinite, perfectly periodic solid composed of a self-repeating sequence of two layers, each made of a homogeneous, rate-independent material, with initial thicknesses H_m and H_f. The solid is deformed under finite plane strain conditions in the X_1–X_2 plane.

is presented relative to a fixed Cartesian coordinate system X_1–X_2, where X_1 is the direction aligned with the direction of lamination in the reference configuration.

In the absence of body forces and inertia effects, the incremental equilibrium equations and interface conditions are

$$\dot{\Pi}_{ij,i} = 0; \quad X_1 \in \Re,\ X_2 \in \{(0, H_{\mathrm{m}}) \cup (H_{\mathrm{m}}, H)\},^{1} \tag{2.1}$$

$$[\![\dot{\Pi}_{2i}]\!] = 0, \quad [\![v_i]\!] = 0; \quad X_1 \in \Re,\ X_2 \in \{0, H_{\mathrm{m}}, H\}, \tag{2.2}$$

where $\dot{\mathbf{\Pi}}$ is the rate of the first Piola–Kirchhoff stress tensor, $\mathbf{v}$ is the displacement rate field and $H = H_{\mathrm{m}} + H_{\mathrm{f}}$ is the initial thickness of the unit cell. Moreover, $[\![f]\!]$ denotes a difference in the values of any field quantity f when evaluated on both sides of an interface.

For any rate-independent, incrementally linear material, the constitutive law can be written in the following form:

$$\dot{\Pi}_{ji}(\lambda, \mathbf{X}) = L_{ijkl}(\lambda, \mathbf{X})\dot{F}_{kl}; \quad \dot{F}_{kl} = v_{k,l}, \tag{2.3}$$

where $\mathbf{L}$ is the incremental (tangent) moduli tensor relating the rate of the transpose of the first Piola–Kirchhoff stress tensor $\dot{\mathbf{\Pi}}^{\mathrm{T}}$ to the rate of the deformation gradient $\dot{\mathbf{F}}$, its work conjugate quantity.

For the rate-independent, quasi-static loading problems considered, the rate of any field quantity (denoted by a superimposed dot) is this quantity's derivative with respect to a "*time-like*" scalar λ, which increases monotonically from zero with the evolution of the loading process. The scalar λ is thus named the "*loading parameter*", and is assumed to uniquely characterize the current state of the material. The incremental moduli tensor $\mathbf{L}$ is evaluated on the principal equilibrium path, i.e., on the path whose stability is under investigation, and is a function of the material properties and the current state in each layer, and is consequently fully characterized by λ. Explicit expressions for $\mathbf{L}$ in the cases of finite elastic and elastoplastic constitutive models are given at the end of this section. For now it suffices to say that the incremental moduli tensor $\mathbf{L}$ possesses major symmetry $L_{ijkl} = L_{klij}$.

The procedure for determining the onset of the first bifurcation, as λ increases monotonically from zero, hinges on finding a non-trivial solution to the system (2.1)–(2.3) and works as follows: By considering the Fourier transform of the governing equations (2.1)–(2.3) with respect to X_1, the system of linear partial differential equations and interface conditions with piecewise constant coefficients is reduced to the following system of ordinary differential equations and interface conditions in X_2

$$\omega_1^2 L_{i1k1}\hat{v}_k - \mathrm{i}\omega_1(L_{i2k1} + L_{i1k2})\hat{v}_{k,2} - L_{i2k2}\hat{v}_{k,22} = 0, \tag{2.4}$$

$$[\![\mathrm{i}\omega_1 L_{i2k1}\hat{v}_k + L_{i2k2}\hat{v}_{k,2}]\!] = 0, \quad [\![\hat{v}_i]\!] = 0, \tag{2.5}$$

[1] Here and subsequently, Latin indexes range from 1 to 2, unless indicated differently. Einstein's summation convention is implied over repeated indexes. Repeated indexes in parentheses are not summed, unless indicated explicitly.

where $\hat{\mathbf{v}}(X_2)$ is the Fourier transform of $\mathbf{v}(X_1,X_2)$ and the real number ω_1 is the Fourier transform variable corresponding to X_1. It is assumed that the displacement rate field $\mathbf{v}$ is uniformly bounded and has adequate continuity. Note that the Fourier transform $\hat{\mathbf{v}}$ exists in the sense of distributions.

To determine a non-trivial solution $\hat{\mathbf{v}}$ (up to a multiplicative constant), for the periodic system of ordinary differential equations in Eqs. (2.4) and (2.5), the system is solved on just one unit cell together with some additional boundary conditions at its ends $X_2 = 0^+$ and $X_2 = H^+$. These conditions are provided by Floquet's theorem (see Floquet, 1883) which applies to linear systems of ordinary differential equations in X_2, with periodic coefficients (period is the unit cell thickness H), according to which

$$\hat{v}_i(H^+) = \exp(\mathrm{i}\omega_2 H)\hat{v}_i(0^+), \tag{2.6}$$

where the real number ω_2 ($\omega_2 H \in [0, 2\pi)$) is the Floquet parameter of the solution.

The general solution to the system of ordinary differential equations with piecewise constant coefficients (2.4) is found to be in each layer, the sum of four linearly independent partial solutions:

$$\begin{aligned}
\hat{v}_k(X_2) &= \sum_{j=1}^{4} \overset{\mathrm{m}(j)}{C}{}_k \exp\left(\mathrm{i}\omega_1 \overset{\mathrm{m}}{Z}{}_{(j)} X_2\right); \quad X_2 \in (0, H_{\mathrm{m}}),\\
\hat{v}_k(X_2) &= \sum_{j=1}^{4} \overset{\mathrm{f}\,(j)}{C}{}_k \exp\left(\mathrm{i}\omega_1 \overset{\mathrm{f}}{Z}{}_{(j)} X_2\right); \quad X_2 \in (H_{\mathrm{m}}, H),\\
\hat{v}_k(X_2) &= \sum_{j=1}^{4} \overset{\mathrm{m}*(j)}{C}{}_k \exp\left(\mathrm{i}\omega_1 \overset{\mathrm{m}}{Z}{}_{(j)} X_2\right); \quad X_2 \in (H, H + H_{\mathrm{m}}),
\end{aligned} \tag{2.7}$$

where $Z_{(j)}$ (j=1,4) are the four complex roots of the following fourth-order polynomial in Z

$$\det[L_{i2k2}Z^2 + (L_{i2k1} + L_{i1k2})Z + L_{i1k1}] = 0, \tag{2.8}$$

and $\mathbf{C}^{(j)}$ is the eigenvector of the 2×2 matrix shown in brackets in Eq. (2.8) and is associated with the root $Z_{(j)}$. The eigenvector components $C_1^{(j)}$ and $C_2^{(j)}$ are related by

$$C_2^{(j)} = D_{(j)} C_1^{(j)}; \quad D_{(j)} \equiv -\frac{L_{1212}Z_{(j)}^2 + (L_{1211} + L_{1112})Z_{(j)} + L_{1111}}{L_{1222}Z_{(j)}^2 + (L_{1221} + L_{1122})Z_{(j)} + L_{1121}}. \tag{2.9}$$

Note that Eqs. (2.8) and (2.9) are valid for each of the two layers and the superscripts m and f are omitted from these equations in the interest of notational simplicity. The requirement that the roots $Z_{(j)}$ are complex, at least for the loading parameter λ of interest, stems from the assumed strong ellipticity of each layer, i.e., the absence of any localized mode of deformation in each layer for all deformations along the loading paths considered here.

The Fourier transform of the interface conditions (2.5), after substituting Eqs. (2.7) and (2.9), gives the following equations for the coefficients $\overset{\mathrm{m}}{\mathbf{C}}_1$, $\overset{\mathrm{f}}{\mathbf{C}}_1$ and $\overset{\mathrm{m}^*}{\mathbf{C}}_1$ in matrix form:

$$\begin{aligned}
&\overset{\mathrm{m}}{\mathbf{V}}\exp(\mathrm{i}\omega_1\overset{\mathrm{m}}{\mathbf{Z}}H_{\mathrm{m}})\overset{\mathrm{m}}{\mathbf{C}}_1=\overset{\mathrm{f}}{\mathbf{V}}\exp(\mathrm{i}\omega_1\overset{\mathrm{f}}{\mathbf{Z}}H_{\mathrm{m}})\overset{\mathrm{f}}{\mathbf{C}}_1,\\
&\overset{\mathrm{f}}{\mathbf{V}}\exp(\mathrm{i}\omega_1\overset{\mathrm{f}}{\mathbf{Z}}H)\overset{\mathrm{f}}{\mathbf{C}}_1=\overset{\mathrm{m}}{\mathbf{V}}\exp(\mathrm{i}\omega_1\overset{\mathrm{m}}{\mathbf{Z}}H)\overset{\mathrm{m}^*}{\mathbf{C}}_1,
\end{aligned}\tag{2.10}$$

for the interfaces $X_2=H_{\mathrm{m}}$ and $X_2=H_{\mathrm{m}}+H_{\mathrm{f}}=H$, respectively. The components of the 4×4 matrices $\mathbf{V}$ and $\mathbf{Z}$ are defined by

$$\begin{aligned}
&V_{1j}=1,\\
&V_{2j}=D_{(j)},\\
&V_{3j}=L_{1212}Z_{(j)}+L_{1211}+(L_{1222}Z_{(j)}+L_{1221})D_{(j)},\\
&V_{4j}=L_{2212}Z_{(j)}+L_{2211}+(L_{2222}Z_{(j)}+L_{2221})D_{(j)},\\
&Z_{ij}=\begin{cases}Z_{(j)}, & i=j,\\ 0, & i\neq j,\end{cases}
\end{aligned}\tag{2.11}$$

and the four-dimensional vector $\mathbf{D}$ is defined in relation (2.9). The components of the four-dimensional vector $\mathbf{C}_1$ are the constants $C_1^{(j)}$ introduced in Eq. (2.7). Here again, the superscripts m and f are omitted from Eq. (2.11) in the interest of notational simplicity and the components of $\mathbf{V}$, $\mathbf{Z}$ and $\mathbf{C}_1$ are evaluated for the corresponding layer.

Substituting Eq. (2.7) into the Floquet conditions (2.6) results in the additional relation

$$\overset{\mathrm{m}^*}{\mathbf{C}}_1=\exp(\mathrm{i}\omega_2H)\exp(-\mathrm{i}\omega_1\overset{\mathrm{m}}{\mathbf{Z}}H)\overset{\mathrm{m}}{\mathbf{C}}_1.\tag{2.12}$$

Finally, after employing the above result (2.12) into Eqs. (2.10), a non-trivial solution $\mathbf{v}(\mathbf{X})\neq0$ (or equivalently $\overset{\mathrm{m}}{\mathbf{C}}_1\neq0$) exists if the matrix with constant coefficients $\mathbf{K}$ has unimodular eigenvalues, i.e.,

$$\begin{aligned}
&\det[\mathbf{K}(\lambda,\omega_1H)-\exp(\mathrm{i}\omega_2H)\mathbf{I}]=0,\\
&\mathbf{K}\equiv\overset{\mathrm{f}}{\mathbf{K}}\overset{\mathrm{m}}{\mathbf{K}},\quad \overset{l}{\mathbf{K}}\equiv\overset{l}{\mathbf{V}}\exp(\mathrm{i}\omega_1\overset{l}{\mathbf{Z}}H_l)\overset{l}{\mathbf{V}}{}^{-1},\quad l=\mathrm{m},\mathrm{f},
\end{aligned}\tag{2.13}$$

where $\mathbf{I}$ is the 4×4 identity matrix. It should be noted here that the 4×4 matrix $\mathbf{K}$ is in general complex in view of the complex roots $Z_{(j)}$ in Eq. (2.8).

Thus, the critical loading parameter λ_{c}, which represents the first occurrence of a bifurcation in the layered solid during a monotonically increasing loading history, corresponds to the first occurrence of a singular matrix in Eq. $(2.13)_1$, as the loading parameter λ increases from zero, for some pair of dimensionless wavenumbers $\omega_1^{\mathrm{c}}H$ and $\omega_2^{\mathrm{c}}H$.

The calculation works as follows: At criticality $y_c \equiv \exp(i\omega_2^c H)$ is an eigenvalue of matrix $\mathbf{K}$, and in view of the fact that y_c is unimodular ($\|y_c\| = 1$), it corresponds to the first occurrence of a root with magnitude plus or minus one of the following characteristic equation:

$$y^4 - I_1^K y^3 + I_2^K y^2 - I_3^K y + I_4^K = 0, \quad I_j^K = I_j^K(\lambda, \omega_1 H), \tag{2.14}$$

where the four invariants I_j^K of matrix $\mathbf{K}$, introduced in Eq. $(2.13)_2$, are in general complex and are defined by

$$\begin{aligned} I_1^K &\equiv \operatorname{tr} \mathbf{K}, \\ I_2^K &\equiv \frac{1}{2}[(\operatorname{tr} \mathbf{K})^2 - \operatorname{tr} \mathbf{K}^2], \\ I_3^K &\equiv \det \mathbf{K} \operatorname{tr} \mathbf{K}^{-1}, \\ I_4^K &\equiv \det \mathbf{K}. \end{aligned} \tag{2.15}$$

For a fixed dimensionless wavenumber $\omega_1 H$, $\hat{\lambda}(\omega_1 H)$ corresponds to the first unimodular root of characteristic equation (2.14). The critical loading parameter λ_c is then found by a numerical search as the minimum loading parameter $\hat{\lambda}(\omega_1 H)$, when the minimum is taken over an adequately large interval $\omega_1 H$, in the process also giving the corresponding critical dimensionless wavenumber $\omega_1^c H$, i.e.,

$$\lambda_c \equiv \min_{\omega_1 H} \hat{\lambda}(\omega_1 H) = \hat{\lambda}(\omega_1^c H). \tag{2.16}$$

For the case of purely orthotropic loading, it can be shown that the four invariants are real and the interested reader is refered to Geymonat et al. (1993) for a more detailed discussion. Here it suffices to say that the four invariants have the following property, which follows from their definitions,

$$I_j^K(\lambda, \omega_1 H) = \operatorname{conj}[I_j^K(\lambda, -\omega_1 H)].^2 \tag{2.17}$$

This property implies that $\hat{\lambda}(\omega_1 H) = \hat{\lambda}(-\omega_1 H)$ and thus justifies the need to scan only the domain $[0, \infty)$ for the dimensionless wavenumber $\omega_1 H$, when searching for the critical loading parameter λ_c.

It should be noted here, that in all the previous calculations it was tacitly assumed that the dimensionless wavenumber $\omega_1 H \neq 0$. The function $\hat{\lambda}(\omega_1 H)$ has a singular point at the origin, i.e., $\hat{\lambda}(0) \neq \hat{\lambda}(\omega_1 H \to 0)$, since two physically different types of modes can exist in the neighborhood of $\omega_1 H = 0$, as described next.

For the case that $\omega_1 H = 0$, i.e., for the modes independent on X_1, the critical loading parameter λ_c can still be found from the transformed governing Eqs. (2.4) and (2.5). In this case it can be seen from Eq. (2.4), that $\hat{v}_1(X_2)$ and $\hat{v}_2(X_2)$ are piecewise linear functions in X_2 within each layer. Applying the interface (2.5) and boundary

[2] Here, conj f denotes the complex conjugate of f. The more common overline notation is avoided in view of its subsequent use for denoting the averaged quantities over the unit cell.

(2.6) conditions results in the following implicit algebraic equation for the loading parameter λ,

$$\det[H_{\mathrm{f}}\overset{\mathrm{m}}{L}_{i2k2}(\lambda)+H_{\mathrm{m}}\overset{\mathrm{f}}{L}_{i2k2}(\lambda)]=0. \tag{2.18}$$

The critical loading parameter λ_{c} corresponds to the first occurrence of a singular matrix in Eq. (2.18) as the loading parameter λ increases from zero. The above equation (2.18) is obtained for the critical dimensionless number $\omega_2^{\mathrm{c}}H=0$ (the choice $\omega_2 H\neq 0,2\pi$ is shown to be impossible) and corresponds to a periodic solution for $\hat{\mathbf{v}}(X_2)$, with period the unit cell thickness H.

Unlike the case $\omega_1 H=0$, which also implies that $\omega_2^{\mathrm{c}}H=0$ and corresponds to a periodic mode, the case $\omega_1 H\to 0$ corresponds to a long-wavelength type mode, when compared to the unit cell size, thus explaining the singularity of $\hat{\lambda}(\omega_1 H)$ in the neighborhood of $\omega_1 H=0$. For this case it has been shown by Geymonat et al. (1993), that the limit value of the critical loading parameter λ_{c}, as $\omega_1 H\to 0$, corresponds to the first loss of ellipticity of the homogenized incremental moduli $\mathbf{L}^H$, which is calculated by solving the appropriate boundary value problem on the unit cell. Derivation of the homogenized incremental moduli $\mathbf{L}^H$ for the layered composites is shown in detail in Geymonat et al. (1993), but for reasons of completeness, a brief outline is presented here. The required homogenized incremental moduli $\mathbf{L}^H$ are obtained by using the method of multiple scales expansion and are found to be

$$L^H_{ijkl}(\lambda)=\frac{1}{H}\int_0^H L_{mnpq}(\delta_{im}\delta_{jn}+\overset{ij}{\varphi}_{m,n})(\delta_{kp}\delta_{lq}+\overset{kl}{\varphi}_{p,q})\,\mathrm{d}X_2, \tag{2.19}$$

where δ_{ij} is the Kronecker delta. The characteristic field $\overset{ij}{\varphi}(X_2)$ is the unit cell's response to the ijth component of the unit macroscopic deformation and is a periodic function in X_2, with period the unit cell thickness H. It is calculated by solving the following boundary value problem given in its variational form:

$$\int_0^H L_{mnpq}(\delta_{kp}\delta_{lq}+\overset{kl}{\varphi}_{p,q})\delta\varphi_{m,n}\,\mathrm{d}X_2=0. \tag{2.20}$$

The first loss of ellipticity results correspond to the lowest loading parameter λ at which the homogenized incremental moduli $\mathbf{L}^H$ loses positive definiteness along direction $\mathbf{n}$ ($\|\mathbf{n}\|=1$),

$$\det[L^H_{ijkl}(\lambda)n_j n_l]=0, \tag{2.21}$$

with $n_1=\cos\theta$ and $n_2=\sin\theta$, and where $\theta\in[0,2\pi)$.

2.2. Loading paths

To complete the bifurcation problem formulated for the infinite, perfectly periodic solid, the loading paths followed from the undeformed, stress-free configuration are now described. The proposed choice of loading paths is motivated by the desire to simulate the loading conditions used in the combined compression and shear experiments by Vogler et al. (2000).

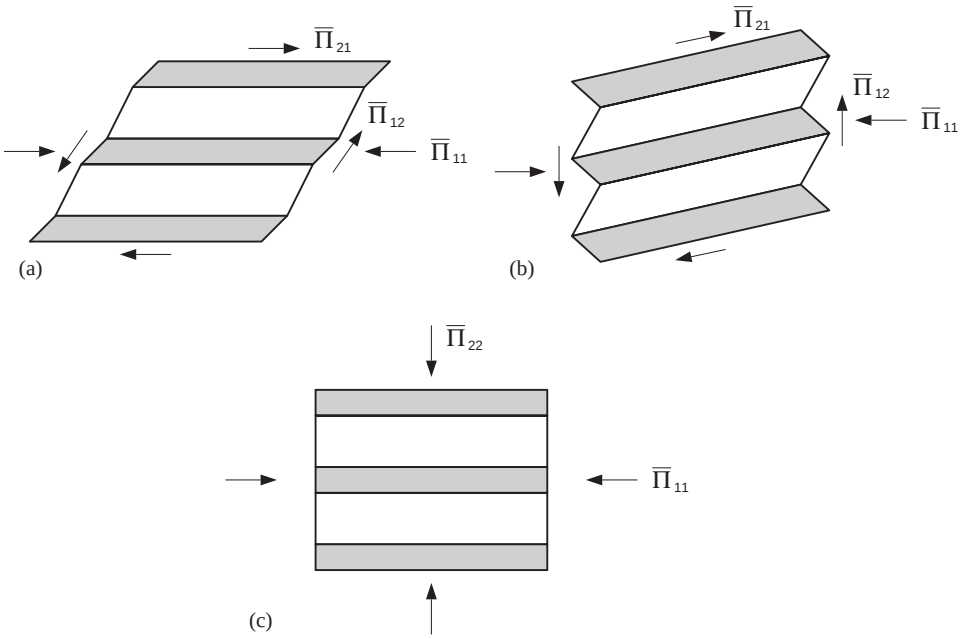

Fig. 2. Schematic representation of an infinite, perfectly periodic solid, subjected to three different states of deformation. The solid is sheared in the direction parallel (a) and normal (b) to the direction of lamination, and is biaxially loaded (c) along the axes of orthotropy.

For each loading path, a combination of the macroscopic (averaged) first Piola–Kirchhoff stress tensor $\bar{\mathbf{\Pi}}$[3] components and their work conjugate, macroscopic (averaged) deformation gradient tensor $\bar{\mathbf{F}}$ components, is prescribed. For the combined axial compression and shear loading, two different states of deformation, depicted in Fig. 2, are considered: In the first and second case, the macroscopic deformation gradient tensor components are $\bar{F}_{21}=0$ and $\bar{F}_{12}=0$, and the composite is sheared in the directions parallel and normal to the direction of lamination so that the prescribed macroscopic first Piola–Kirchhoff stress tensor components are related by $\bar{\Pi}_{21}/\bar{\Pi}_{11}=-\tan\phi$ and $\bar{\Pi}_{12}/\bar{\Pi}_{11}=-\tan\phi$, respectively. For completeness of the investigation, an orthotropic loading path is considered in the third case, with its macroscopic first Piola–Kirchhoff stress tensor components related by $\bar{\Pi}_{22}/\bar{\Pi}_{11}=-\tan\phi$. The ratio of the macroscopic first Piola–Kirchhoff stress tensor components $\tan\phi$ is kept fixed for proportional loading paths.

Since the macroscopic force parameter Λ, which is a measure of the macroscopic stress magnitude and is defined immediately below, reaches a maximum for the

[3] Here and subsequently, the overline symbol denotes an averaged quantity over the unit cell and is not to be confused with the more common notation for a complex conjugate quantity. Thus, if f is any field quantity, then $\bar{f}=\frac{1}{H}\int_0^H f\,\mathrm{d}X_2$.

majority of loading paths considered, its work conjugate quantity Δ is prescribed instead and thus plays the role of the monotonically increasing loading parameter λ. The calculation of the macroscopic loading parameter $\lambda \equiv \Delta$ is described in the following subsections, in which the methodology for obtaining the principal equilibrium solution and consequently the incremental moduli $\mathbf{L}$ is given for both the finitely elastic and rate-independent elastoplastic composites.

Finally one additional remark about the principal solutions which correspond to all the loading paths is in order. Due to the homogeneous properties of each layer, the resulting stresses and strains are constant within each layer.

2.2.1. Finite elasticity

For the layerwise homogeneous composite considered in this work, which is subjected to a uniform state of deformation, the macroscopic (averaged) strain energy density $\bar{W}$ can be written in the following form:

$$\bar{W}(\bar{\mathbf{F}}) = \frac{1}{H}\int_0^H W(X_2, \mathbf{F}(X_2))\,\mathrm{d}X_2 = \xi_{\mathrm{m}} \overset{\mathrm{m}}{W}(\overset{\mathrm{m}}{\mathbf{F}}) + \xi_{\mathrm{f}} \overset{\mathrm{f}}{W}(\overset{\mathrm{f}}{\mathbf{F}}),$$

$$\xi_l \equiv \frac{H_l}{H}, \quad l = \mathrm{m}, \mathrm{f}, \tag{2.22}$$

where $\overset{\mathrm{m}}{W}(\overset{\mathrm{m}}{\mathbf{F}})$ and $\overset{\mathrm{f}}{W}(\overset{\mathrm{f}}{\mathbf{F}})$ are the matrix and fiber strain energy densities, and ξ_{m} and ξ_{f} are the matrix and fiber volume ratios, respectively.

For the reason explained previously, instead of prescribing the macroscopic force parameter Λ, its dimensionless, work conjugate quantity Δ is prescribed instead. The macroscopic force parameter Λ is then found from the requirement that

$$\bar{\Pi}_{ji}(\bar{F}_{ij} - \delta_{ij}) = \Lambda\Delta; \quad \bar{\Pi}_{ji} = \Lambda \overset{\circ}{\bar{\Pi}}_{ji}, \tag{2.23}$$

where the components of $\overset{\circ}{\bar{\mathbf{\Pi}}}$ are prescribed and depend on the loading path. For the mixed loading considered in this work, the macroscopic deformation gradient tensor component $\bar{F}_{21} = 0$ or $\bar{F}_{12} = 0$ is also prescribed and corresponds to shearing in the direction parallel or normal to the direction of lamination.

In the absence of body forces, the equilibrium equations and in turn the principal equilibrium solution for the infinite, layered solid are obtained by minimizing the macroscopic strain energy density $\bar{W}$ with respect to the macroscopic deformation gradient tensor $\bar{\mathbf{F}}$, subject to the constraint (2.23). The constrained minimization problem is equivalent to minimizing with respect to the local (within layer) deformation gradient tensors $\overset{\mathrm{m}}{\mathbf{F}}$ and $\overset{\mathrm{f}}{\mathbf{F}}$, and is formulated with a numerical solution algorithm in mind using the penalty approach

$$\min_{\overset{\mathrm{m}}{F}_{kl}, \overset{\mathrm{f}}{F}_{kl}} \{\xi_{\mathrm{m}} \overset{\mathrm{m}}{W}(\overset{\mathrm{m}}{\mathbf{F}}) + \xi_{\mathrm{f}} \overset{\mathrm{f}}{W}(\overset{\mathrm{f}}{\mathbf{F}}) + \frac{1}{2\zeta}[\overset{\circ}{\bar{\Pi}}_{ji}(\bar{F}_{ij} - \delta_{ij}) - \Delta]^2\}, \tag{2.24}$$

where ζ $(0 < \zeta \ll 1)$ is the penalty parameter. The macroscopic and local deformation gradient tensors are related using geometric considerations and are found to be

$$\bar{F}_{11} = \overset{\mathrm{m}}{F}_{11} = \overset{\mathrm{f}}{F}_{11},$$

$$\bar{F}_{12} = \xi_{\mathrm{m}} \overset{\mathrm{m}}{F}_{12} + \xi_{\mathrm{f}} \overset{\mathrm{f}}{F}_{12},$$

$$\bar{F}_{21} = \overset{\mathrm{m}}{F}_{21} = \overset{\mathrm{f}}{F}_{21},$$

$$\bar{F}_{22} = \xi_{\mathrm{m}} \overset{\mathrm{m}}{F}_{22} + \xi_{\mathrm{f}} \overset{\mathrm{f}}{F}_{22}. \tag{2.25}$$

The layerwise equilibrium equations obtained from Eq. (2.24) are more conveniently written in the following variational form:

$$\int_0^H \left[\xi_{\mathrm{m}} \frac{\partial \overset{\mathrm{m}}{W}}{\partial \overset{\mathrm{m}}{F}_{kl}} \delta \overset{\mathrm{m}}{F}_{kl} + \xi_{\mathrm{f}} \frac{\partial \overset{\mathrm{f}}{W}}{\partial \overset{\mathrm{f}}{F}_{kl}} \delta \overset{\mathrm{f}}{F}_{kl} - \Lambda \overset{\circ}{\bar{\Pi}}_{ji} \left(\frac{\partial \bar{F}_{ij}}{\partial \overset{\mathrm{m}}{F}_{kl}} \delta \overset{\mathrm{m}}{F}_{kl} + \frac{\partial \bar{F}_{ij}}{\partial \overset{\mathrm{f}}{F}_{kl}} \delta \overset{\mathrm{f}}{F}_{kl} \right) \right] \mathrm{d}X_2 = 0, \tag{2.26}$$

where the macroscopic force parameter Λ is calculated by

$$\Lambda = -\frac{1}{\zeta} [\overset{\circ}{\bar{\Pi}}_{ji} (\bar{F}_{ij} - \delta_{ij}) - \Delta]. \tag{2.27}$$

2.2.2. Elastoplasticity

Observe that the variational form of equilibrium equations in Eq. (2.26) can alternatively be written in terms of the local (within each layer) first Piola–Kirchhoff stress tensor as follows:

$$\int_0^H \left[\xi_{\mathrm{m}} \overset{\mathrm{m}}{\Pi}_{lk} \delta \overset{\mathrm{m}}{F}_{kl} + \xi_{\mathrm{f}} \overset{\mathrm{f}}{\Pi}_{lk} \delta \overset{\mathrm{f}}{F}_{kl} - \Lambda \overset{\circ}{\bar{\Pi}}_{ji} \left(\frac{\partial \bar{F}_{ij}}{\partial \overset{\mathrm{m}}{F}_{kl}} \delta \overset{\mathrm{m}}{F}_{kl} + \frac{\partial \bar{F}_{ij}}{\partial \overset{\mathrm{f}}{F}_{kl}} \delta \overset{\mathrm{f}}{F}_{kl} \right) \right] \mathrm{d}X_2 = 0, \tag{2.28}$$

after considering that for finite elasticity $\Pi_{ji} = \partial W / \partial F_{ij}$.

Taking the rate of the equilibrium equations (2.28) results in the incremental equilibrium equations required for the rate-independent, elastoplastic, layered solid, and they are

$$\int_0^H \left[\xi_{\mathrm{m}} \dot{\overset{\mathrm{m}}{\Pi}}_{lk} \delta \overset{\mathrm{m}}{F}_{kl} + \xi_{\mathrm{f}} \dot{\overset{\mathrm{f}}{\Pi}}_{lk} \delta \overset{\mathrm{f}}{F}_{kl} - \dot{\Lambda} \overset{\circ}{\bar{\Pi}}_{ji} \left(\frac{\partial \bar{F}_{ij}}{\partial \overset{\mathrm{m}}{F}_{kl}} \delta \overset{\mathrm{m}}{F}_{kl} + \frac{\partial \bar{F}_{ij}}{\partial \overset{\mathrm{f}}{F}_{kl}} \delta \overset{\mathrm{f}}{F}_{kl} \right) \right] \mathrm{d}X_2 = 0, \tag{2.29}$$

since for the loading paths considered $(\partial \bar{F}_{ij} / \partial F_{kl})^{\cdot} = 0$, in view of Eq. (2.25).

The additional relation for calculating the rate of the macroscopic force parameter $\dot{\Lambda}$ is obtained by taking the rate of the requirement (2.23), and is found to be

$$\overset{\circ}{\bar{\Pi}}_{ji} \dot{\bar{F}}_{ij} = \dot{\Delta}, \tag{2.30}$$

where $\dot{\Delta} = 1$ for all the numerical calculations in Section 3.

2.3. Constitutive laws

The analysis presented thus far is valid for any homogeneous, rate-independent, incrementally linear material model. As mentioned previously, two different types of

layered composites are discussed. The first composite is made of two alternating layers of compressible foam rubbers and the second is a graphite–epoxy (AS4/PEEK) composite which was extensively studied, experimentally and theoretically, under combined compression and shear loading by Vogler et al. (2000). A specific choice of material models is now proposed for the numerical calculations presented in Section 3.

2.3.1. Hyperelastic material

The hyperelastic material used to model a compressible foam rubber is the standard Blatz–Ko material (see Blatz and Ko, 1962). For plane strain deformations considered in this work, the strain energy density W is of the following form:

$$W = \frac{\mu}{2}\left(\frac{J_1}{J_2} + 2\sqrt{J_2} - 4\right), \tag{2.31}$$

where μ is the initial shear modulus of the material and J_i $(i = 1,2)$ are the two invariants of the right Cauchy–Green tensor $C_{ij} = F_{ki}F_{kj}$, where $\mathbf{F}$ is the deformation gradient tensor, and they are

$$J_1 = \operatorname{tr}\mathbf{C}, \quad J_2 = \frac{1}{2}[(\operatorname{tr}\mathbf{C})^2 - \operatorname{tr}\mathbf{C}^2]. \tag{2.32}$$

For any hyperelastic material, the incremental moduli tensor $\mathbf{L}$ required by the general bifurcation analysis and first introduced in Eq. (2.3) is

$$L_{ijkl} = \frac{\partial^2 W}{\partial F_{ij}\partial F_{kl}}, \tag{2.33}$$

and the first Piola–Kirchhoff stress tensor $\mathbf{\Pi}$ is

$$\Pi_{ji} = \frac{\partial W}{\partial F_{ij}}, \tag{2.34}$$

with the partial derivatives evaluated on the principal equilibrium path. The specific values of the initial shear modulus μ, for each of the two layers, are given in Section 3.

2.3.2. Elastoplastic material

The inelastic matrix studied in the combined compression and shear failure tests by Vogler et al. (2000) is modeled using two different rate-independent elastoplastic models, namely, the finite strain versions of the isotropic J_2 deformation and flow theory materials, both sharing the same experimentally obtained uniaxial stress–strain curve.

The incremental moduli tensor $\mathbf{L}$, expressed in the full Lagrangian formulation (see Abeyaratne and Triantafyllidis, 1981 for the pertaining moduli derivation) required by the general bifurcation analysis, is given by

$$L_{ijkl} = \mathscr{L}_{ijkl} - \frac{1}{2}(S_{ik}C^{-1}_{jl} + S_{il}C^{-1}_{jk} + S_{jk}C^{-1}_{il} - S_{jl}C^{-1}_{ik}), \quad i,j,k,l = 1,3,^4 \tag{2.35}$$

where $\mathbf{S}$ is the second Piola–Kirchhoff stress tensor and $\mathbf{C}^{-1}$ is the inverse of the right Cauchy–Green tensor. The incremental moduli tensor $\mathscr{L}$, relating the Jaumann rate of

[4] Here and also in Eqs. (2.36) and (2.38), Latin indexes range from 1 to 3.

the Kirchhoff stress tensor $\overset{\nabla}{\boldsymbol{\tau}}$ to the strain rate tensor $\mathbf{D}$, its work conjugate quantity, is of the form

$$\mathscr{L}_{ijkl} = \frac{E^*}{1+\nu^*}\left[\frac{1}{2}\left(C^{-1}_{ik}C^{-1}_{jl} + C^{-1}_{il}C^{-1}_{jk}\right) + \frac{\nu^*}{1-2\nu^*}\,C^{-1}_{ij}C^{-1}_{kl} - \frac{3}{2}\,\frac{(E^*/E_t)-1}{(E^*/E_t)-(1-2\nu^*)/3}\,\frac{S'_{ij}S'_{kl}}{\tau_e^2}\right], \tag{2.36}$$

where for deformation theory: $E^* = E_s$ and $\nu^* = \nu_s$, and for flow theory: $E^* = E$ and $\nu^* = \nu$.

In the above expressions, E and ν are the elastic Young's modulus and the elastic Poisson's ratio of the material's uniaxial response, respectively. In addition, the secant modulus E_s, the tangent modulus E_t and the secant Poisson's ratio ν_s are defined by the following expressions:

$$E_s = \frac{\tau}{\varepsilon}, \quad E_t = \frac{d\tau}{d\varepsilon}, \quad \nu_s = \frac{1}{2} - \frac{E_s}{E}\left(\frac{1}{2} - \nu\right), \tag{2.37}$$

in terms of the material's uniaxial Kirchhoff stress τ and the natural (logarithmic) strain ε response. It should be mentioned at this point that the incremental moduli $\mathscr{L}$ in Eq. (2.36) assume that the material is in the plastic regime, i.e., $\tau \geqslant \tau_y$, where τ_y is the uniaxial yield stress. The uniaxial Kirchhoff stress τ in the expressions for E_s, E_t and ν_s in $\mathscr{L}$ is replaced by the equivalent Kirchhoff stress τ_e, which is given in terms of the deviatoric second Piola–Kirchhoff stress tensor $\mathbf{S}'$ by

$$\tau_e^2 = \frac{3}{2}\,S'_{ij}S'_{ij}; \quad S'_{ij} = S_{ij} - \tfrac{1}{3}\,C^{-1}_{ij}S_{kl}C_{kl}. \tag{2.38}$$

All the above expressions (2.35)–(2.38) are valid for an arbitrary uniaxial stress–strain response. The material's uniaxial response used in the numerical calculations presented in Section 3 is obtained experimentally and the interested reader is refered for a detailed procedure to Vogler et al. (2000). Also, note that the fibers are assumed to be isotropic and linearly elastic, and their material properties are also obtained experimentally.

Some general remarks are in order at this point. The finite strain version of the J_2 deformation theory of plasticity, introduced by Stören and Rice (1975), has its advantages as a constitutive choice, over its flow counterpart, due to the merits for predicting experimental results for stability problems involving proportional loading paths. The interested reader is referred to the review article by Hutchinson (1974), for an extensive and detailed discussion of this subject. In Section 3, the numerical results for the stability predictions of the graphite–epoxy (AS4/PEEK) composite are compared for both theories of plasticity for all the loading paths considered, i.e., for the mixed proportional as well as non-proportional loading paths.

3. Numerical calculations and discussion

The present section pertains to the numerical application of the bifurcation problem for the layered solid presented in Section 2. The section is divided into two parts. A

description of the numerical algorithms, followed by the material and geometry data used in the calculations, is given in the first part. The second part of the section is devoted to the presentation and discussion of the obtained results.

3.1. Numerical calculations

The critical force Λ_c and displacement Δ_c parameters, at the onset of first bifurcation, and the corresponding critical dimensionless wavenumbers $\omega_1^c H$ and $\omega_2^c H$ are obtained from the characteristic equation (2.14), whose construction involves calculation of the stress state $\mathbf{\Pi}(\Delta)$ within each layer. In addition the force and displacement parameters corresponding to the maximum force and to the first loss of ellipticity of the homogenized incremental moduli $\mathbf{L}^H$ are also found. The numerical calculation of the stress state at displacement parameter Δ is done differently for the hyperelastic and elastoplastic materials, as it is detailed immediately below.

3.1.1. Hyperelastic material

The layerwise equilibrium equations and in turn the principal equilibrium solution are obtained as a result of the constrained minimization problem (2.24). This non-linear system of equilibrium equations is solved numerically using a straightforward incremental Newton–Raphson solution procedure. A typical increment size of the displacement parameter Δ which is used in the solution of the equilibrium equations is 10^{-4}. The penalty parameter ζ introduced in the constrained minimization problem (2.24) is taken to be 10^{-8}. The solution is found to be insensitive to ζ when lower values of the penalty parameter are considered.

The results for the hyperelastic material correspond to the initial fiber to matrix shear modulus ratio of $\mu_f/\mu_m = 10^2$, and are normalized with respect to $\mu_f = 1$. As a result Λ/μ_f is dimensionless.

3.1.2. Elastoplastic material

For the elastoplastic material, the calculation of the principal solution is based on the system of first-order ordinary differential equations, with respect to the displacement parameter Δ, which are obtained from the incremental equilibrium equations (2.29) and from the additional requirement (2.30), where the incremental moduli are given by Eqs. (2.35)–(2.38). The equations are numerically integrated using a standard fourth-order Runge–Kutta method with a step size equal to 10^{-5} of the displacement parameter Δ.

The parameters required for the description of the uniaxial stress–strain response, of the inelastic matrix and linearly elastic fiber, are obtained experimentally by Vogler et al. (2000). The uniaxial stress–strain curve for the epoxy (matrix) is shown in Fig. 3, where τ is the uniaxial Kirchhoff stress (in 10^6 psi) and ε is the natural (logarithmic) strain. The corresponding uniaxial stress–strain constants used in the numerical calculations are: the elastic Young's modulus $E_m = 893$ ksi, the elastic Poisson's ratio $\nu_m = 0.356$ and the uniaxial yield stress $\tau_{my} = 3.515$ ksi. The material parameters for the graphite (fiber), which is assumed to be isotropic and linearly elastic, are: the elastic

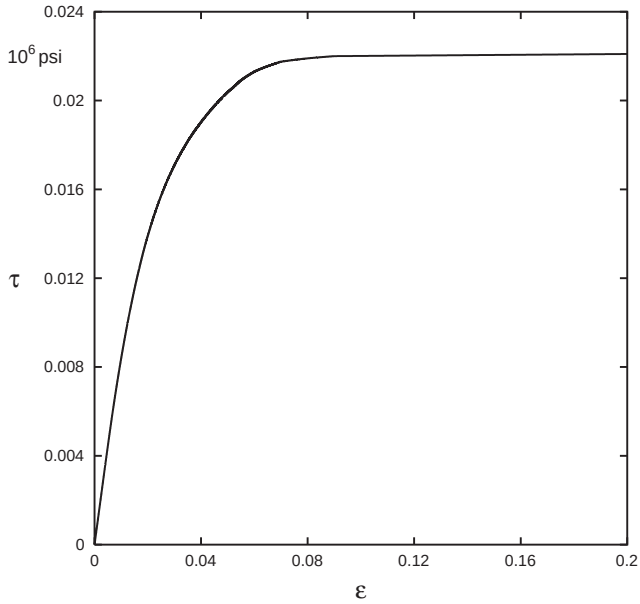

Fig. 3. The uniaxial stress–strain curve for the (PEEK) matrix in the graphite–epoxy composite with a fiber volume ratio $\xi_f = 0.60$, obtained experimentally by Vogler et al. (2000).

Young's modulus $E_f = 31000$ ksi and the elastic Poisson's ratio $\nu_f = 0.263$. As a result of the units chosen, the force parameter Λ has units of psi.

3.2. Results and discussion

The presentation and discussion of results is divided into two main parts. The first part pertains to the composites made of two alternating layers of a compressible foam rubber, each modeled using a Blatz–Ko material, as described in Section 2. The composite with a high fiber volume ratio $\xi_f = 0.60$ (thick fibers) is analyzed first, under proportional loading for the first two types of deformation, depicted in Fig. 2, i.e., for shearing parallel and normal to the direction of lamination. The same analysis is then repeated for a low fiber volume ratio $\xi_f = 0.10$ (thin fibers). This foam rubber composite investigation is concluded by examining the effect of varying fiber volume ratio, in the range $0.10 \leqslant \xi_f \leqslant 0.80$, for shearing parallel to the direction of lamination.

The second part is devoted to the investigation of a particular graphite–epoxy composite, with a fiber volume ratio $\xi_f = 0.60$, which was extensively studied both experimentally and numerically by Vogler et al. (2000). In this case the critical strains are small when compared to the corresponding ones in the finite elasticity application, but the presence of large rotations still requires a full Lagrangian formulation. For this reason the inelastic matrix (epoxy) is modeled using the finite strain versions of the

isotropic J_2 deformation and flow theory materials. The numerical results presented here are for the infinite, perfect composite and comparisons are made with the corresponding results obtained by Vogler et al. (2000), for the finite sized, imperfect specimens. Both versions of the J_2 plasticity theory are compared under proportional as well as non-proportional loading paths for the two types of shear deformation considered. The investigation for the graphite–epoxy composite is concluded by presenting the results for orthotropic loading, again for both versions of the J_2 plasticity theory.

In all the figures shown here, the initial bifurcation curves are plotted in solid lines. The critical load parameter $\lambda_c = \Lambda_c$, which corresponds to the onset of first bifurcation, is found by scanning all the possible non-negative dimensionless wavenumbers $\omega_1 H$ in the X_1 direction. For all the calculations reported, to find the critical load parameter, it is sufficient to scan the space $0 \leqslant \omega_1 H \leqslant 5$ in 0.1 increments. The singularity in the neighborhood of $\omega_1 H = 0$, which corresponds to the loss of macroscopic ellipticity of the composite, is treated according to the discussion in Section 2 (see Eq. (2.21)). The corresponding loss of macroscopic ellipticity curves are plotted in dotted lines and the orientation angle θ is scanned in 1° increments. Finally, the maximum force curves are plotted in dashed lines.

3.2.1. *Compressible foam rubber composite*

The results in Figs. 4 and 5 correspond to a compressible foam rubber composite with a high fiber volume ratio $\xi_f = 0.60$, which is subjected to proportional loading for two types of deformation: shearing parallel and normal to the direction of lamination. In Figs. 4(a) and (b), the results for initial bifurcation, loss of macroscopic ellipticity and maximum force are recorded on the force–displacement curves obtained for different load paths $0 \leqslant \phi \leqslant \pi/2$, plotted in 1° increments. In Fig. 4(a), for shearing parallel to the direction of lamination, there is no maximum force for purely axial compression of an infinite, perfectly periodic solid, corresponding to $\phi = 0$. As the load angle ϕ increases, for $0 < \phi \leqslant \pi/2$, the force parameter Λ is first an increasing function of the displacement parameter Δ, which then passes through a maximum before decreasing. This behavior is expected from the influence of small fiber misalignments on the axially compressed fiber composites (see Argon, 1972), where shear has a destabilizing effect since it reduces the maximum axial load. Notice that the initial bifurcation and loss of macroscopic ellipticity curves are below the maximum force, which means that the bifurcation always occurs before the maximum force is reached. However, the differences are negligible for very strong shearing $\phi > \pi/6$. It is interesting to note that in Fig. 4(b), for shearing normal to the direction of lamination, a maximum force is observed only for very weak shearing $0 < \phi \ll \pi/180$ (see insert). Also, although shear has initially a destabilizing effect, as expected from the previous case, it can also be a stabilizing factor which can be seen from the fact that the critical force parameter Λ_c is not a monotonically decreasing function of Δ. Observe from Figs. 4(a) and (b) that for small values of the load angle ϕ, the onset of failure predictions show similar trends for both types of deformation, while differences become more pronounced for increased shearing, i.e., for large values of ϕ.

The influence of shear can further be seen in Figs. 5(a) and (b) where the normalized critical axial stress $\bar{\Pi}^c_{11}/\mu_f$, corresponding to the initial bifurcation, is plotted as

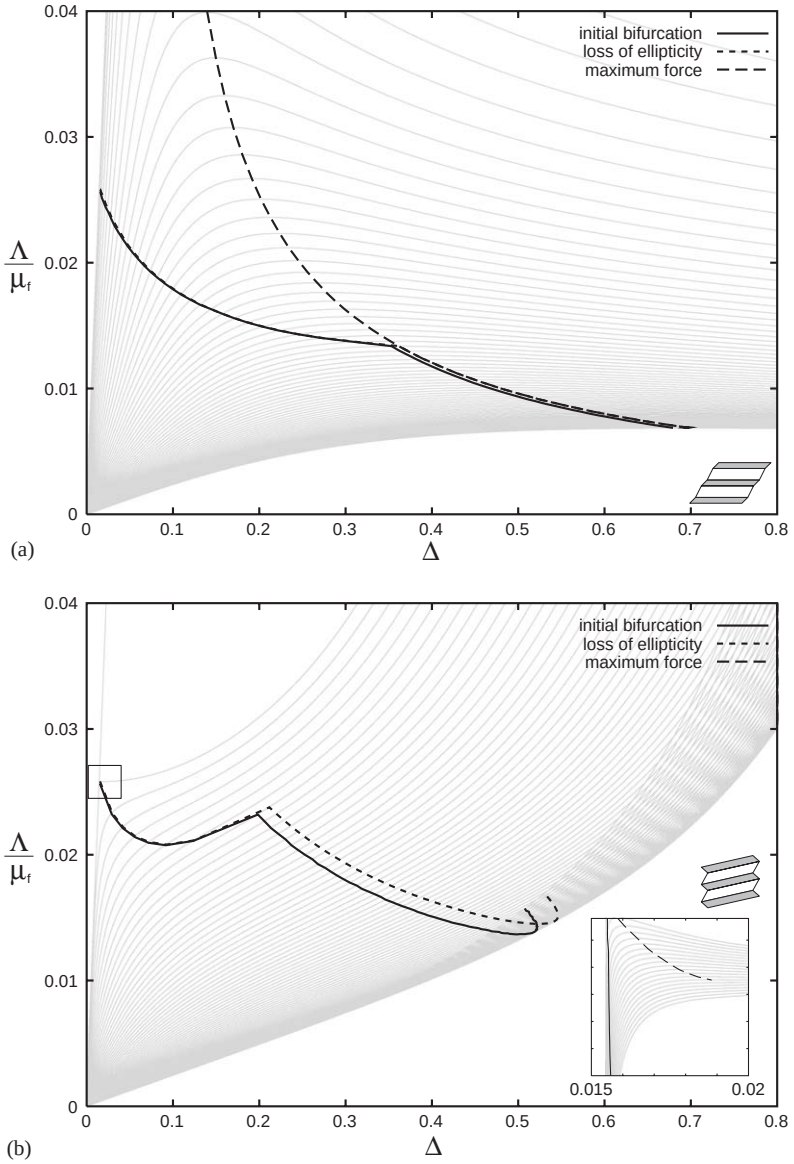

Fig. 4. The onset of bifurcation, loss of ellipticity and maximum force predictions are plotted on the force–displacement curves obtained for $0 \leqslant \phi \leqslant \pi/2$ under proportional loading, for shearing parallel (a) and normal (b) to the direction of lamination. The compressible Blatz–Ko type foam rubber composite has a fiber volume ratio $\xi_f = 0.60$.

a function of the normalized prescribed shear stress. For shearing parallel and normal to the direction of lamination the prescribed shear stresses are $\bar{\Pi}_{21}$ and $\bar{\Pi}_{12}$, respectively. As previously observed in Fig. 5(a), shear parallel to the direction of lamination

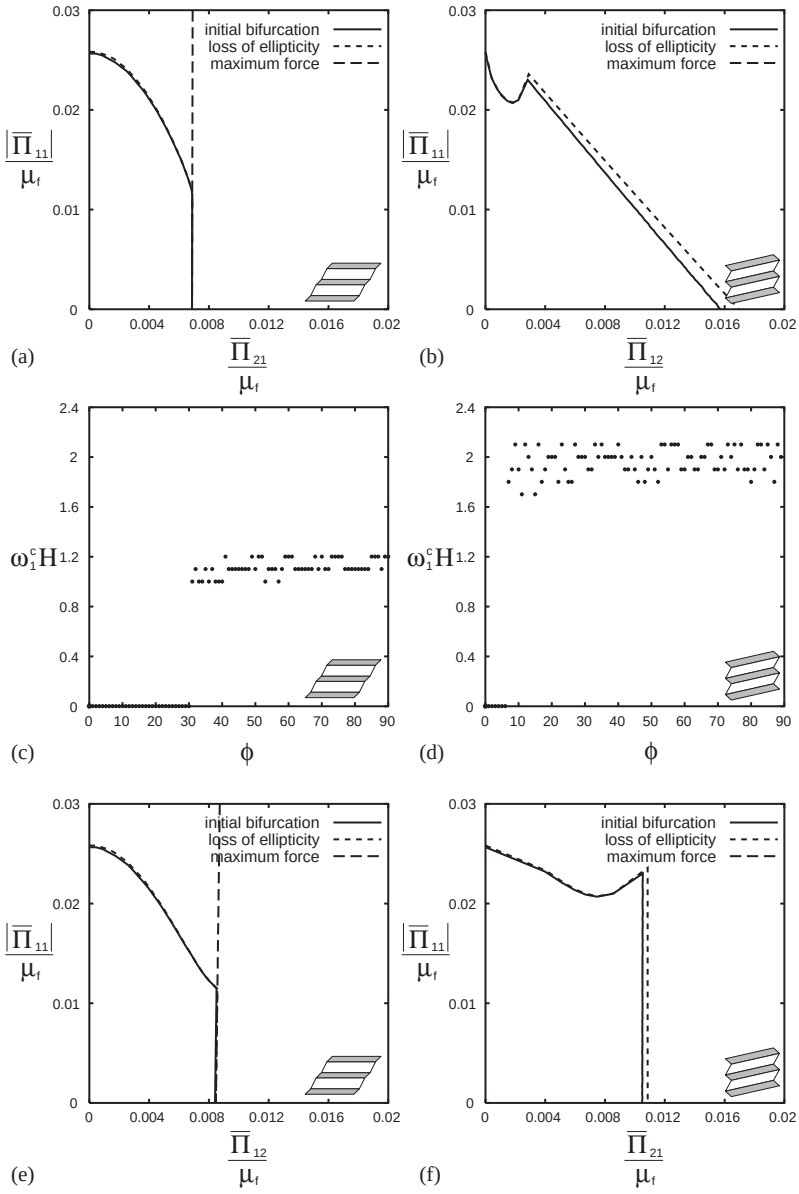

Fig. 5. The onset of failure predictions are obtained for shearing parallel and normal to the direction of lamination. The compressible Blatz–Ko type foam rubber composite has a fiber volume ratio $\xi_f = 0.60$.

has a destabilizing influence and the critical axial stress is a monotonically decreasing function of the prescribed shear stress $\bar{\Pi}_{21}$. From Fig. 5(b), it can be seen that the effect of shear for shearing normal to the direction of lamination is not monotonic,

although initially shearing has a destabilizing effect. In Figs. 5(c) and (d), the critical dimensionless wavenumber $\omega_1^c H$ is plotted in terms of the load angle ϕ and in all the numerical calculations, increment for the dimensionless wavenumber $\omega_1 H$ is 0.1. There is a high sensitivity of the critical dimensionless wavenumber $\omega_1^c H$ to the increment size for the displacement parameter Δ. Observe from Fig. 5(c), that for $0 \leqslant \phi \leqslant \pi/6$, the critical dimensionless wavenumber $\omega_1^c H = 0$, i.e., the initial bifurcation and loss of macroscopic ellipticity results coincide, which means that the critical wavelength is much larger than the unit cell size (long-wavelength type mode). For $\phi > \pi/6$, the critical dimensionless wavenumber $\omega_1^c H$ is finite and thus the initial bifurcation results precede the loss of macroscopic ellipticity results. Similar results can be seen in Fig. 5(d) for shearing normal to the direction of lamination, where the initial bifurcation and loss of macroscopic ellipticity results coincide for a smaller range of load angles $\phi \leqslant \pi/30$. In Figs. 5(e) and (f), the normalized critical axial stress is plotted as a function of the normalized reaction shear stress, which is the work conjugate quantity to the deformation component kept at zero, and shows similar trends to Figs. 5(a) and (b).

The results for a compressible foam rubber composite with a low fiber volume ratio $\xi_f = 0.10$ are presented in the same way as for its high fiber volume counterpart in Figs. 6 and 7. The initial bifurcation and loss of macroscopic ellipticity results are different from the ones obtained for the composite with a high fiber volume ratio $\xi_f = 0.60$. Most notable difference is that for both types of deformation, shearing parallel and normal to the direction of lamination, shear has initially a stabilizing effect, which can be seen by the increase in the critical force and displacement for increasing load angle ϕ in Figs. 6(a) and (b). For shearing parallel to the direction of lamination the initial bifurcation and loss of macroscopic ellipticity results coincide initially, but later diverge, while for shearing normal to the direction of lamination the initial bifurcation always occurs before the loss of macroscopic ellipticity, thus indicating the absence of the long-wavelength type mode of instability for any load path. Another difference is that for shearing normal to the direction of lamination, see Fig. 6(b), no maximum force is observed for small values of the load angle $\phi \approx 0$, which is in contrast with the results for the high fiber volume case in Fig. 4(b). The non-monotonic dependence of the critical axial stress on shear stress can clearly be seen in Figs. 7(a) and (b), where the critical axial stress is first an increasing function of the prescribed shear stress, which then passes through a maximum before decreasing. Note that in Fig. 7(b), for shearing in the direction normal to the direction of lamination, the initial bifurcation curve in stress space is well inside the loss of macroscopic ellipticity curve for all the load angles ϕ. This can also be seen from Fig. 7(d), where in contrast to Fig. 7(c), the critical dimensionless wavenumber $\omega_1^c H$ is always finite. Here again, Figs. 7(e) and (f) depict the normalized critical axial stress plotted as a function of the normalized reaction shear stress and show similar behavior to Figs. 7(a) and (b).

Finally, in Fig. 8, the influence of varying fiber volume ratio ξ_f on the initial bifurcation is examined for a compressible foam rubber composite, which is sheared parallel to the direction of lamination for three different load paths. In Figs. 8(a) and (b), the normalized critical axial stress $\bar{\Pi}_{11}^c/\mu_f$ and the critical dimensionless wavenumber $\omega_1^c H$ are plotted as functions of the fiber volume ratio ξ_f for $\phi = 0$ (uniaxial

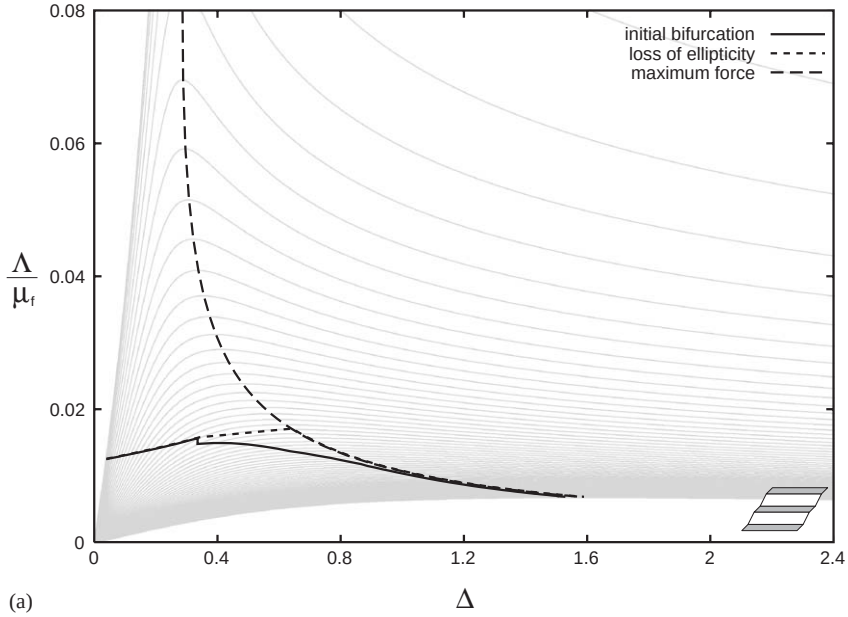

(a)

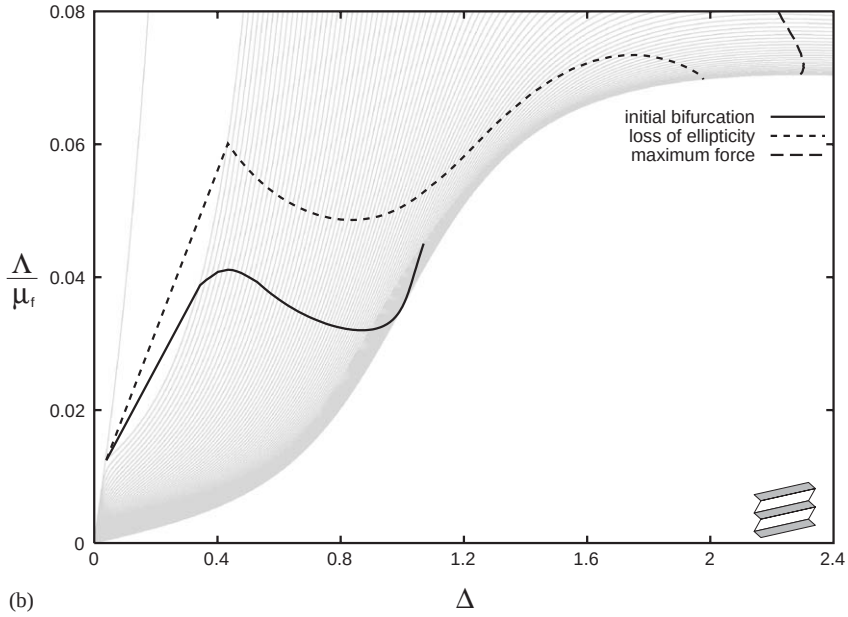

(b)

Fig. 6. The onset of bifurcation, loss of ellipticity and maximum force predictions are plotted on the force–displacement curves obtained for $0 \leqslant \phi \leqslant \pi/2$ under proportional loading, for shearing parallel (a) and normal (b) to the direction of lamination. The compressible Blatz–Ko type foam rubber composite has a fiber volume ratio $\xi_f = 0.10$.

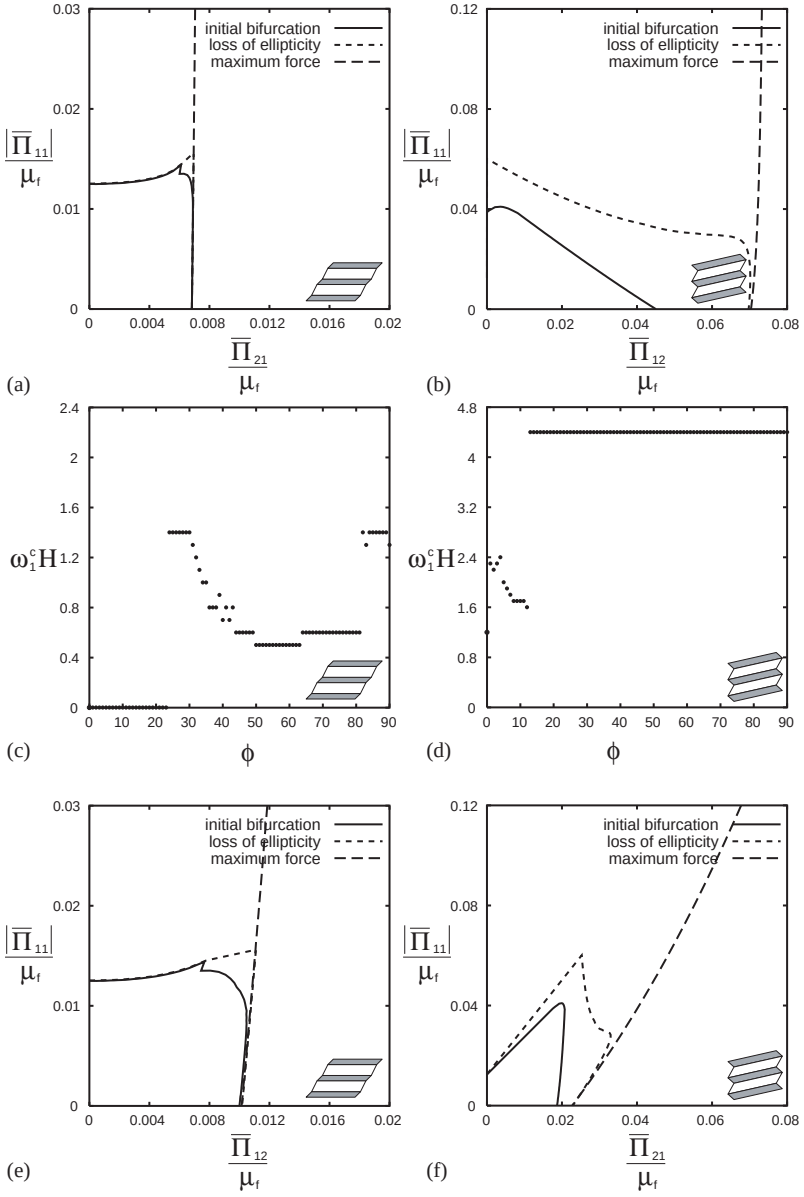

Fig. 7. The onset of failure predictions are obtained for shearing parallel and normal to the direction of lamination. The compressible Blatz–Ko type foam rubber composite has a fiber volume ratio $\xi_f = 0.10$.

compression). Observe that the critical axial stress is a monotonically increasing function of the fiber volume ratio for $0.1 \leqslant \xi_f \leqslant 0.8$, and that the critical dimensionless wavenumber $\omega_1^c H = 0$, indicating a global (long-wavelength type) critical mode. These

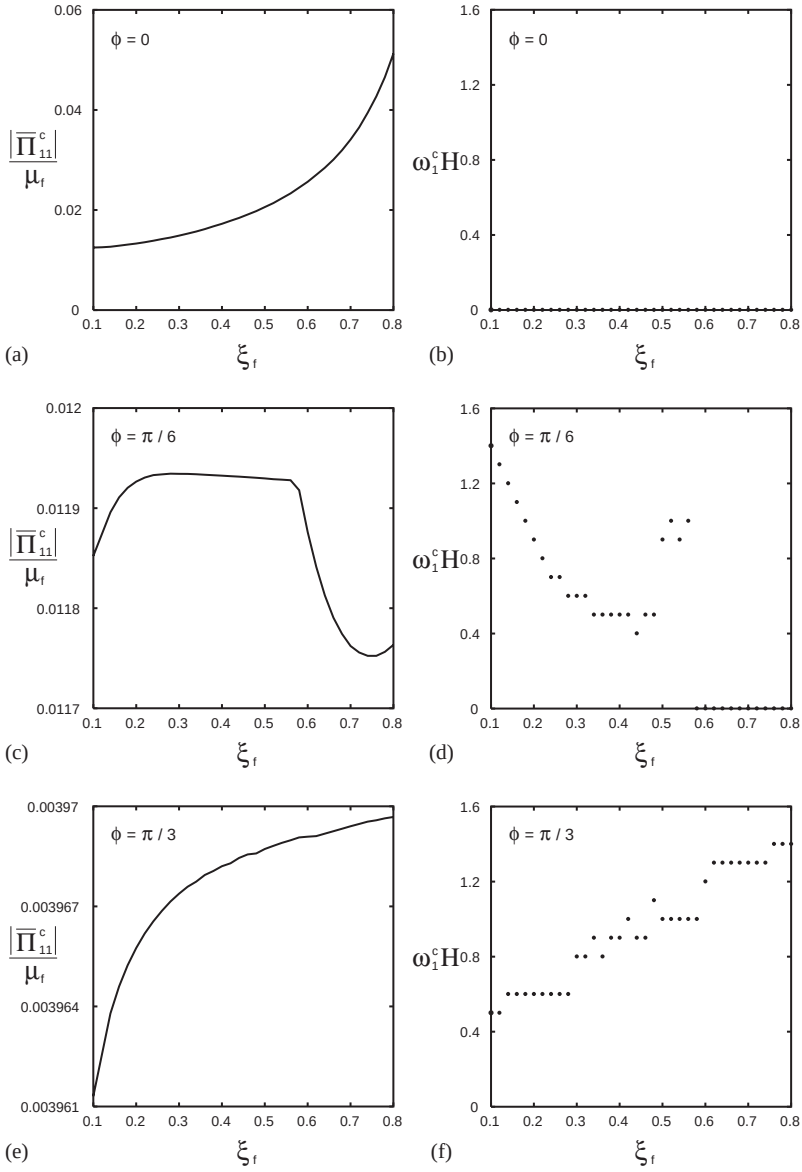

Fig. 8. The initial bifurcation predictions for the normalized axial stress $\bar{\Pi}^c_{11}/\mu_f$ are plotted as functions of the fiber volume ratio ξ_f, for the load angles $\phi = 0$, $\pi/6$ and $\pi/3$, and are obtained for shearing parallel to the direction of lamination in a compressible Blatz-Ko foam rubber composite.

results agree with the previous finding by Triantafyllidis and Bardenhagen (1996), which show that in compression the critical dimensionless wavenumber $\omega_1^c H \neq 0$ only for very low fiber volume ratio $\xi_f < 0.1$. Figs. 8(c) and (d) are plotted for a different

loading path $\phi=\pi/6$. Here one can see that the critical axial stress is first an increasing function of the fiber volume ratio ξ_f, which then passes through a maximum, decreases and then increases again. Note that now for the fiber volume ratio $0.1 \leqslant \xi_f \leqslant 0.56$, the critical dimensionless wavenumber $\omega_1^c H$ is finite, indicating a local critical mode, while for higher fiber volume ratio $\xi_f > 0.56$ the critical mode is global. Figs. 8(e) and (f) are plotted for $\phi=\pi/3$ and the critical axial stress is again a monotonically increasing function of the fiber volume ratio ξ_f, the difference with $\phi=0$ being that for this loading path the critical dimensionless wavenumber $\omega_1^c H$ is always finite, i.e., the critical mode is always local.

3.2.2. Graphite–epoxy composite

Continuing in the format used for the compressible foam rubber composite, the results in Figs. 9 and 10 are presented for a graphite–epoxy composite with a fiber volume ratio $\xi_f = 0.60$, whose inelastic matrix is modeled using the isotropic J_2 deformation theory of plasticity. The composite is again subjected to proportional loading for the same two types of combined axial compression and shear deformation. In Figs. 9(a) and (b), the initial bifurcation, loss of macroscopic ellipticity and maximum force results are recorded on the force–displacement parameter curves obtained for different load paths $0 \leqslant \phi \leqslant \pi/2$. For shearing parallel to the direction of lamination, Fig. 9(a), the maximum force results are similar in character to their counterparts obtained for the compressible foam rubber composite, but at much smaller strains due to the rapid reduction of the matrix stiffness past the yield strain, which can be seen from the smaller range of relevant values for the displacement parameter Δ. Notice that the force parameter Λ is first an increasing function of the displacement parameter Δ, which after passing through a local maximum and a local minimum, increases again for some load angles ϕ. This increase in the force parameter Λ, at large displacements Δ, is strongly dependent on the material's uniaxial stress–strain response, somewhat arbitrarily chosen for large strains, but not without a lot of thought. The reason for this is that for such large strains ($\varepsilon > 6\%$) there is no experimental data available, to the best of our knowledge. Nevertheless, the choice of $\tau(\varepsilon)$ affects the force–displacement parameter curves well beyond our range of interest, since the initial bifurcation and loss of macroscopic ellipticity results always occur before the maximum force for all the load angles ϕ. The critical force parameter Λ_c is a monotonically decreasing function of the displacement Δ, with respect to the load angle ϕ, showing a destabilizing effect of shear. One difference for shearing normal to the direction of lamination, Fig. 9(b), is that a maximum force is observed only for weak shearing $0 < \phi < 2\pi/45$, in which range it also coincides with the initial bifurcation and loss of macroscopic ellipticity results. Also, for $\phi \geqslant 2\pi/45$, the results for initial bifurcation and loss of macroscopic ellipticity are substantially different.

The destabilizing influence of shear on the critical axial stress $\bar{\Pi}_{11}^c$ can further be seen in Figs. 10(a) and (b), where the critical axial stress corresponding to the initial bifurcation is a monotonically decreasing function of the prescribed shear stresses, $\bar{\Pi}_{21}$ and $\bar{\Pi}_{12}$, for shearing parallel and normal to the direction of lamination. It is important to note that for both types of deformation, the critical dimensionless wavenumber $\omega_1^c H = 0$, i.e., the critical wavelength is much larger than the unit cell size,

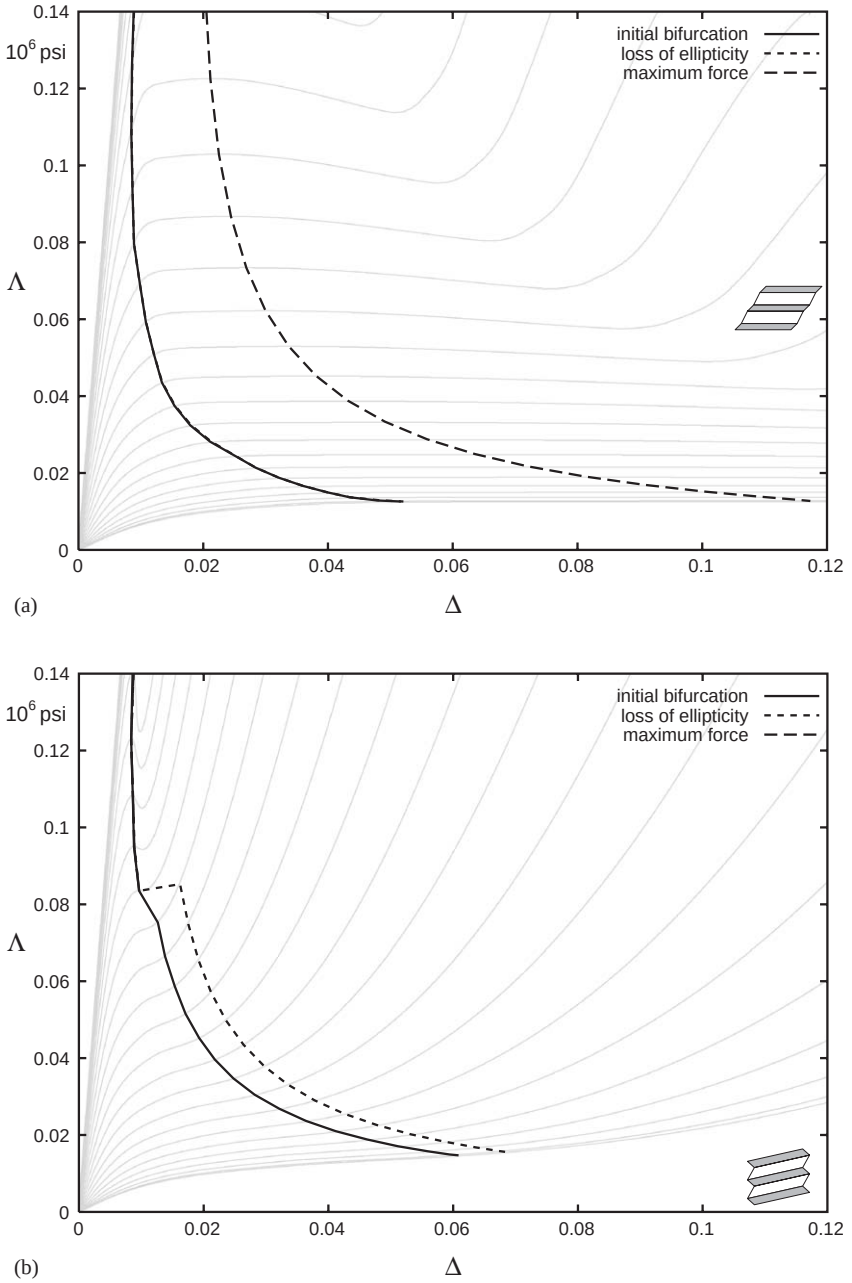

Fig. 9. The onset of bifurcation, loss of ellipticity and maximum force predictions are plotted on the force–displacement curves obtained for $0 \leqslant \phi \leqslant \pi/2$ under proportional loading, for shearing parallel (a) and normal (b) to the direction of lamination. The matrix in the graphite–epoxy composite with a fiber volume ratio $\xi_f = 0.60$ is modeled using the isotropic J_2 deformation theory of plasticity.

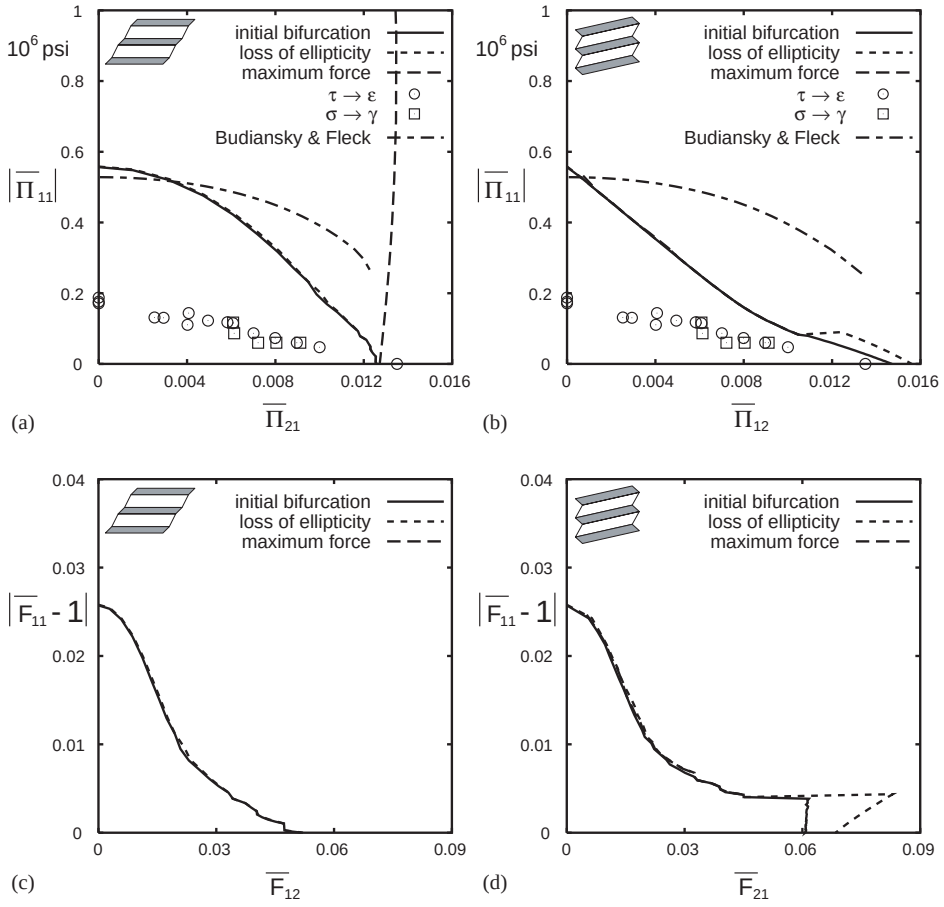

Fig. 10. The onset of failure surfaces in stress and strain space are obtained for shearing parallel and normal to the direction of lamination. The numerical results are superposed to the experimentally obtained results by Vogler et al. (2000) and compared to the approximate model by Budiansky and Fleck (1993). The matrix in the graphite–epoxy composite with a fiber volume ratio $\xi_f = 0.60$ is modeled using the isotropic J_2 deformation theory of plasticity.

except for very strong shearing normal to the direction of lamination $\phi \geqslant 2\pi/45$, in Fig. 10(b). New addition here is that our numerical results have been superposed to the experimentally obtained results by Vogler et al. (2000) for the compressive strength (defined as a limit load) under shear loading. Contrary to the imperfect, finite sized specimen, examined by Vogler et al. (2000), our model is infinite, perfectly periodic and deforms under plane strain. Although the trend is the same, the numerical values obtained for the critical axial stress are much higher than their experimental counterparts due to a strong imperfection sensitivity. It is now well known that fiber imperfections have a decisive role in the compressive strength of aligned fiber composites which

was first recognized by Argon (1972). Calculations show that the onset of bifurcation results for a perfect structure are an upper bound for the results for a real, imperfect structure, which are of the limit load type. Observe from Figs. 10(c) and (d), that the critical axial deformation gradient $\bar{F}_{11}^{c}$ is also a monotonically decreasing function of the shear deformation gradients, $\bar{F}_{12}$ and $\bar{F}_{21}$, respectively.

It is of interest to compare our exact two-dimensional continuum mechanics results with the predictions of an approximate structural model by Budiansky and Fleck (1993), which are also included in Figs. 10(a) and (b). The bifurcation-buckling stress for a perfectly aligned composite with straight fibers, is obtained by assuming the fibers to be linearly elastic and the matrix to follow a J_2 deformation theory model. In this case the critical axial stress $\bar{\Pi}_{11}^{c}$ is calculated by solving (iteratively) the following system of equations:

$$\bar{\Pi}_{11}^{c} = \frac{G_m}{(1-\xi_f)\left[1+3G_m\left(\frac{1}{E_{ms}(\tau_e)}-\frac{1}{E_m}\right)\right]}; \quad (\tau_e)^2 = (\overset{m}{\Pi}_{11})^2 + 3(\tau_m)^2,$$

$$\bar{\Pi}_{11}^{c} = \left[(1-\xi_f)+\xi_f\frac{E_f}{E_{ms}(\tau_e)}\right]\overset{m}{\Pi}_{11}, \tag{3.1}$$

where G_m and $E_{ms}(\tau_e)$ are the elastic shear modulus and the secant modulus of the matrix material, respectively. The shear stress τ_m in the expression for the equivalent stress in the matrix τ_e is equal to the prescribed shear stress $\overset{m}{\Pi}_{21}$ or $\overset{m}{\Pi}_{12}$, for shearing parallel or normal to the direction of lamination. Observe from Figs. 10(a) and (b) that for both types of deformation, our results for weak shearing, i.e., for low values of the load angle ϕ, are in very good agreement with the theoretical predictions by Budiansky and Fleck (1993). For progressively stronger shearing, their predictions increasingly overestimate our results, but a comparison in this range is not meaningful, given the fact that their work assumes small strains and low shear. Also note, that their methodology cannot predict the influence of shear on the critical axial stress when the flow theories with smooth yield surfaces are used to model the matrix material, because the effective, initial shear modulus remains equal to its elastic value. In this case the predictions by Budiansky and Fleck (1993) reduce to the well-known formula by Rosen (1965).

The results for the same graphite–epoxy composite, but when the inelastic matrix is modeled using the isotropic J_2 flow theory of plasticity, are presented in Figs. 11 and 12. The most notable difference, when compared to the deformation theory results, is that for shearing parallel to the direction of lamination, Fig. 11(a), no maximum force is observed. To this end, the lack of available uniaxial stress–strain data at high strains has an influence on the force–displacement curves. Nevertheless, the results for the initial bifurcation and loss of macroscopic ellipticity are well within the range of available data, and the critical force parameter Λ_c is still a monotonically decreasing function of the displacement parameter Δ. Notice in Fig. 11(b), that for shearing normal to the direction of lamination, the composite is stable for very strong shearing, i.e., there is no bifurcation and no loss of macroscopic ellipticity for $\phi \geqslant 2\pi/45$. In Figs. 12(a) and (b), the numerical results for the critical axial stress, as a function of the prescribed shear stress, are again superposed to the experimentally obtained results by Vogler et al. (2000). The difference between the results is greater than in the case

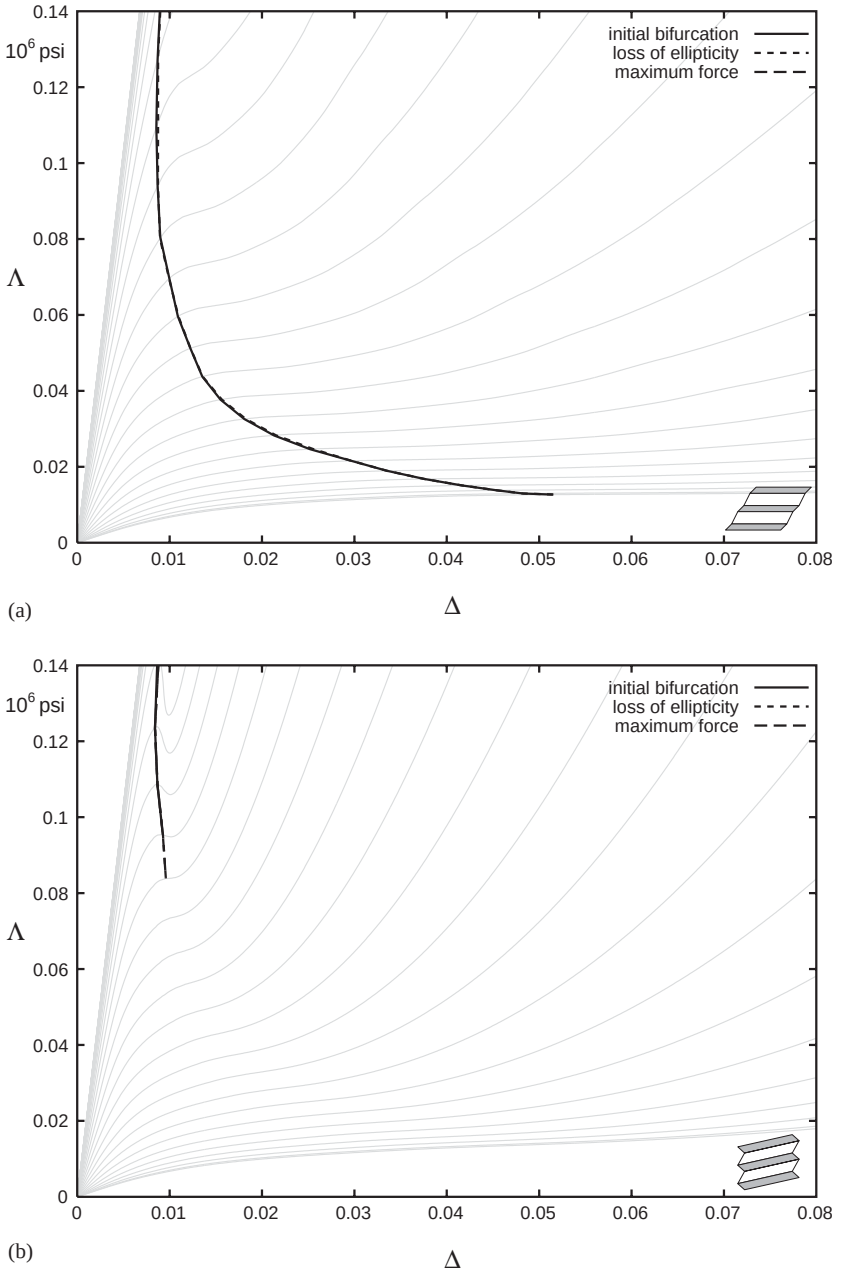

Fig. 11. The onset of bifurcation, loss of ellipticity and maximum force predictions are plotted on the force–displacement curves obtained for $0 \leqslant \phi \leqslant \pi/2$ under proportional loading, for shearing parallel (a) and normal (b) to the direction of lamination. The matrix in the graphite–epoxy composite with a fiber volume ratio $\xi_f = 0.60$ is modeled using the isotropic J_2 flow theory of plasticity.

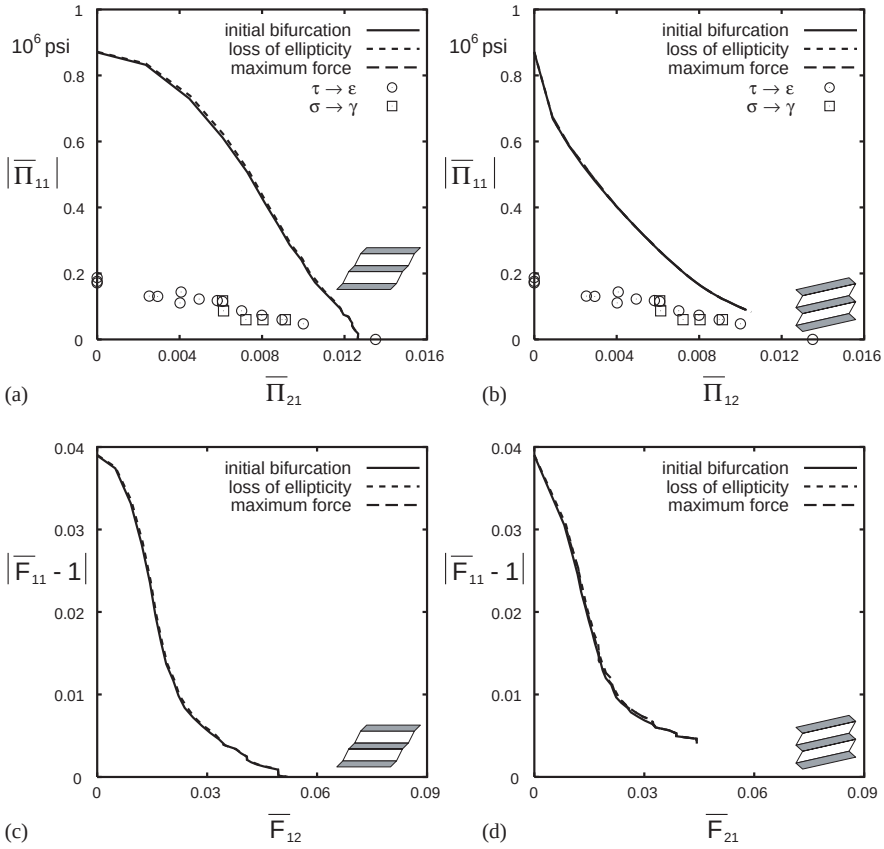

Fig. 12. The onset of failure surfaces in stress and strain space are obtained for shearing parallel and normal to the direction of lamination. The numerical results are superposed to the experimentally obtained results by Vogler et al. (2000). The matrix in the graphite–epoxy composite with a fiber volume ratio $\xi_f = 0.60$ is modeled using the isotropic J_2 flow theory of plasticity.

of deformation theory. This finding is expected in view of the well-known advantages of the deformation theory of plasticity versus its flow counterpart for predicting more realistically the experimental results involving proportional loading. The results for the critical axial deformation gradient $\bar{F}^c_{11}$, as a function of the shear deformation gradients corresponding to the two types of deformation, are plotted in Figs. 12(c) and (d), and have similar character to the results obtained using the deformation theory of plasticity.

The influence of proportional and non-proportional loading on the onset of bifurcation for the same graphite–epoxy composite are compared in Fig. 13 using the J_2 deformation and flow theories of plasticity. Only the results obtained for shearing parallel to the direction of lamination are presented and due to the high fiber volume ratio the critical dimensionless wavenumber $\omega^c_1 H = 0$ for all the load angles ϕ. The

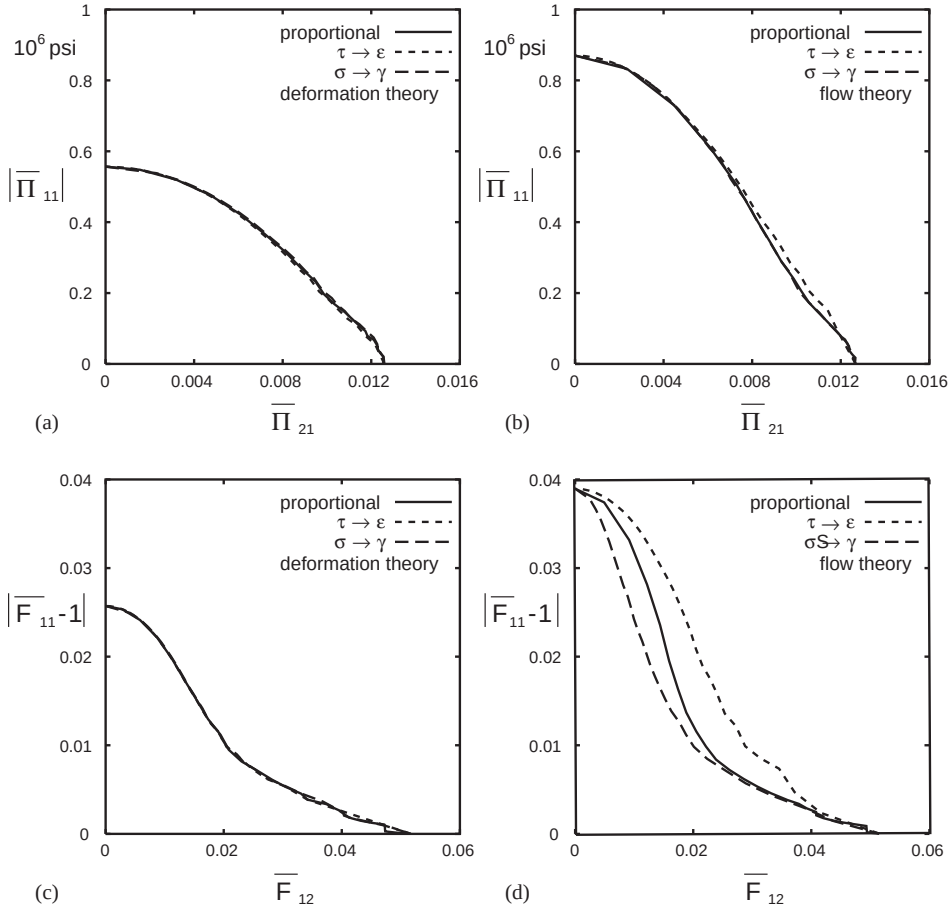

Fig. 13. The onset of bifurcation surfaces in stress and strain space are obtained for shearing parallel to the direction of lamination, under proportional and non-proportional loading paths. The matrix in the graphite–epoxy composite with a fiber volume ratio $\xi_f = 0.60$ is modeled using the isotropic J_2 deformation and flow theory of plasticity.

two non-proportional loading paths considered are similar to loading in Vogler et al. (2000) and they are: The composite is first sheared to a predetermined level, which is then held fixed while the composite is compressed axially. Similarly, for the other loading path, the composite is first compressed axially to a predetermined level, which is then held fixed while the composite is sheared. Observe from Figs. 13(a) and (b), that for both plasticity theories there is virtually no difference in the results for the onset of failure surface in stress space, for all three loading paths considered. This also holds true for the onset of failure surface in strain space, when the deformation theory is used in Fig. 13(c), but for the flow theory used in Fig. 13(d), some difference in the results is observed. Nevertheless, this confirms the finding of Vogler et al. (2000),

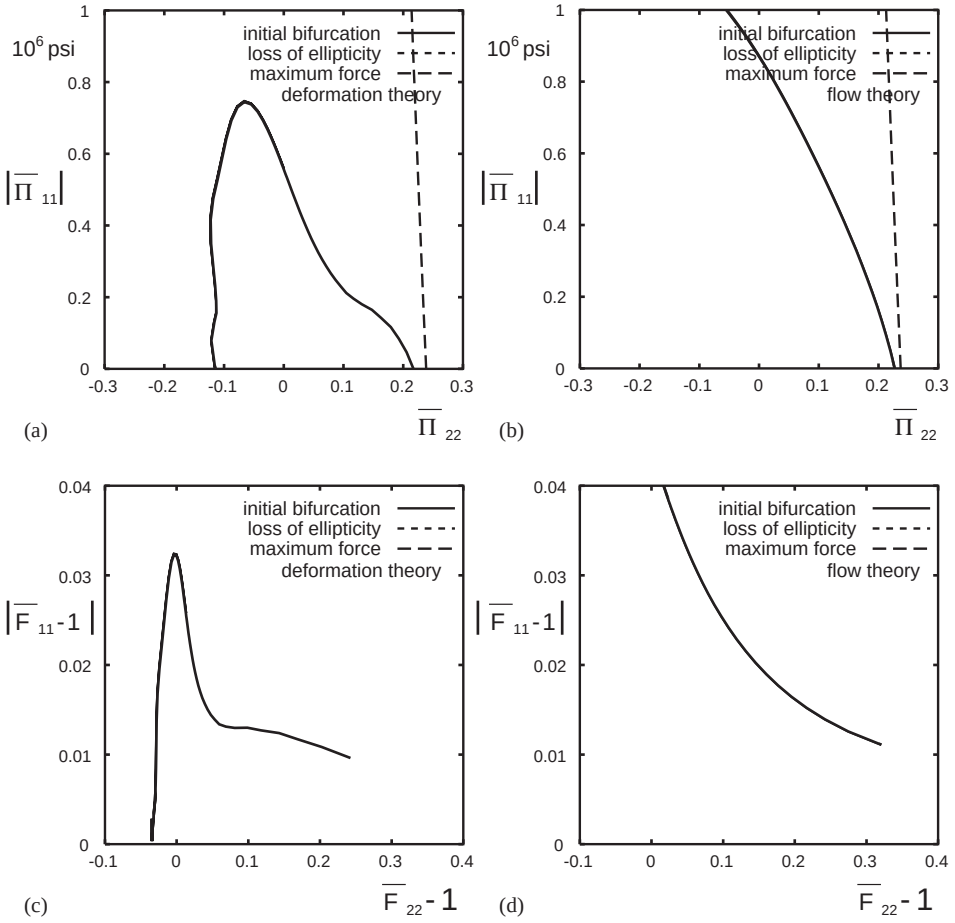

Fig. 14. The onset of failure surfaces in stress and strain space are obtained for biaxial loading along the axes of orthotropy, under proportional loading paths. The matrix in the graphite–epoxy composite with a fiber volume ratio $\xi_f = 0.60$ is modeled using the isotropic J_2 deformation and flow theory of plasticity.

that no significant difference for the failure stresses is observed for different loading paths.

The numerical investigation is concluded by presenting the results for the graphite–epoxy composite, subjected to proportional orthotropic loading in Fig. 14. The results are presented for the isotropic J_2 deformation and flow theories of plasticity. For both theories the initial bifurcation and loss of macroscopic ellipticity occur before the maximum force, and the critical dimensionless wavenumber $\omega_1^c H = 0$. In Figs. 14(a) and (b), the critical axial stress $\bar{\Pi}_{11}^c$ is plotted as a function of the compressive as well as tensile loading, normal to the direction of lamination $-\pi/2 \leqslant \phi \leqslant \pi/2$. Observe that for the deformation theory results in Fig. 14(a), the critical axial stress is a monotonically decreasing function of the normal stress $\bar{\Pi}_{22}$ for tension, while for compression it is

first an increasing function, which then passes through a maximum before decreasing. For the flow theory presented in Fig. 14(b), the results for tension have similar character when compared to the results for the deformation theory, but for compression the critical axial stress is always a monotonically increasing function of the normal stress. Similarly in Figs. 14(c) and (d), a non-monotonic dependence of the critical axial deformation gradient $\bar{F}^{c}_{11}$ is observed for the deformation theory, while for the flow theory the critical axial deformation gradient is a monotonic function of the normal deformation gradient $\bar{F}_{22}$.

It should be emphasized at this point, that all the numerical calculations presented in this work correspond to the onset of bifurcation in infinite, layered solids. Investigation of the post-buckling response of these solids is a completely different and more difficult problem from the onset of instability problem addressed here. It is the post-buckling response that determines the practical load carrying capacity of these solids. The reader interested in numerical modeling of the post-buckling behavior of actual fiber-reinforced composites is referred to a work by Kyriakides et al. (1995).

4. Conclusion

Failure under axial compression, due to the bifurcation buckling type of instability at the microscopic level, is a major limiting factor in the use and design of fiber-reinforced composite materials. Moreover, macroscopic failure stresses are extremely sensitive to the load orientation, since even a small amount of shear significantly reduces the critical axial compressive stress.

Although the onset of instability mechanism is local in nature, it is experimentally impossible to avoid the simultaneous influence of finite boundaries and material imperfections on failure. In addition, the consideration of a general load path with arbitrary macroscopic load orientation, even though very important for practical applications, is another major experimental stumbling block. The present work is motivated by the above-mentioned experimental difficulties combined with the absence of exact finite strain continuum mechanics models (in spite of the abundance of very good structural approximations) for studying the onset of instability in rate-independent, perfect, fiber-reinforced composites of infinite extent under finite strains and subjected to arbitrary macroscopic load orientations. The onset of instability is modeled as a bifurcation from the straight fiber configuration and in general it corresponds to a local type mode, whose wavelength is commensurate with the unit cell size. When the first instability corresponds to a global type mode, whose wavelength is much larger than the unit cell size, the instability can be detected from the macroscopic properties as the first loss of ellipticity of the homogenized moduli of the composite. In addition to the stability information, the presence of a maximum load in the principal solution has been calculated for two composites: the first composite is made of two alternating layers of a very stiff and very soft compressible rubber and the other is a graphite–epoxy (AS4/PEEK) composite, whose material properties have been determined experimentally.

The results show a strong sensitivity of the initial bifurcation, loss of macroscopic ellipticity and maximum load predictions to the load orientation, i.e., to the ratio of the

macroscopic shear to normal stress. For the composite made of two alternating layers of a compressible foam rubber (with one layer being two orders of magnitude stiffer than the other), it has been determined that a bifurcated solution always exists prior to reaching a maximum load. There is no maximum load for pure uniaxial compression in the fiber direction, but a small amount of shear results in a maximum load along a loading path. Also, for strong shearing, the critical dimensionless wavenumber $\omega_1^c H$ is always finite, indicating that the initial bifurcation precedes the loss of macroscopic ellipticity. Moreover, shear can have a stabilizing as well as a destabilizing effect, depending on both the fiber volume ratio ξ_f and the load orientation.

Similar results are obtained for the graphite–epoxy composite, the main difference being that shear always has a destabilizing effect, regardless of the load orientation. Although the maximum load still cannot be reached for uniaxial compression in the fiber direction, for the fiber volume ratio ξ_f considered, it can now occur concurrently with the initial bifurcation and loss of macroscopic ellipticity. Moreover, the mode corresponding to the critical dimensionless wavenumber $\omega_1^c H$ is in general of the long-wavelength type. This coincidence of the micro-failure and macro-failure implies that a macroscopic localization mode will occur for the post-buckling deformation (see discussion in Triantafyllidis and Bardenhagen, 1996). This is in agreement with the experiments by Vogler et al. (2000), where the observed failure mode leads to a kink band type instability. Our calculations show no significant path dependence, which is also in agreement with their experiments.

Some additional comments are in order at this point about the proposed failure concepts. Unlike the previous theoretical and experimental studies on the failure in periodic composites, the present study considers all possible macroscopic load orientations. The onset of failure predictions are calculated for perfect microstructures and thus provide a consistent upper bound for the failure loads of the corresponding actual composites. The imperfections in the geometry and material properties of the microstructure result in failure surfaces which are nested inside their counterparts for the perfect case (see Triantafyllidis and Schraad, 1998 for the case of aluminum honeycombs) as seen from our present comparisons to the experimental data of Vogler et al. (2000). Moreover, the proposed approach gives us the possibility of investigating all possible macroscopic load orientations, a task which presents considerable experimental difficulties. Since the failure predictions show a strong dependence on the macroscopic load orientation, the proposed methodology offers a useful tool for designing appropriate microstructures. An additional result stemming from the finite strain formulation, is that the direction of shear loading (parallel or normal to the direction of lamination) plays an important role in the stability of layered composites.

Finally, it should be emphasized here that the methodology used in this work to predict the onset of failure in layered composites, is applicable to any infinite, perfectly periodic, rate-independent solid which undergoes finite deformations. The ideas used here are currently being employed to investigate the stability of fiber-reinforced composites by using three-dimensional microstructural models. This direction seems to be the next logical step in applying the results of the present investigation to engineering problems involving the failure of microstructured media under arbitrary multi-axial loading and in the absence of imperfections and finite boundaries.

Acknowledgements

This work was supported by AFOSR under Grant F49620-99-1-0098 to the University of Michigan. The authors would like to acknowledge many helpful discussions with Professor S. Kyriakides from the University of Texas at Austin, who also made available to us his work on the material characterization of AS4/PEEK composite, which was used in our elastoplastic model.

References

Abeyaratne, R., Triantafyllidis, N., 1981. Emergence of shear bands in plane strain. Int. J. Solids Struct. 17, 1113–1134.

Argon, A.S., 1972. Fracture of composites. In: Herman, H. (Ed.), Treatise on Material Science and Technology, 1. Academic Press, New York.

Blatz, P.J., Ko, W.L., 1962. Application of finite elastic theory to the deformation of rubbery materials. Trans. Soc. Rheol. 6, 223–251.

Budiansky, B., 1983. Micromechanics. Comput. Struct. 16, 3–12.

Budiansky, B., Fleck, N.A., 1993. Compressive failure of fiber composites. J. Mech. Phys. Solids 41, 183–211.

Cohen, Y., Albalak, R.J., Dair, B.J., Capel, M.S., Thomas, E.L., 2000. Deformation of oriented lamellar block copolymer films. Macromolecules 33, 6502–6516.

Floquet, G., 1883. Sur les équations différentielles linéaires à coefficients périodiques. Ann. Sci. École Norm. Sup. 12, 47–89.

Geymonat, G., Müller, S., Triantafyllidis, N., 1993. Homogenization of nonlinearly elastic materials, microscopic bifurcation and macroscopic loss of rank-one convexity. Arch. Rat. Mech. Anal. 122, 231–290.

Hsu, S.-Y., Vogler, T.J., Kyriakides, S., 1998. Compressive strength predictions for fiber composites. J. Appl. Mech. 65, 7–16.

Hutchinson, J.W., 1974. Plastic buckling. Adv. Appl. Mech. 14, 67–144.

Kyriakides, S., Arseculeratne, R., Perry, E.J., Liechti, K.M., 1995. On the compressive failure of fiber reinforced composites. Int. J. Solids Struct. 32, 689–738.

Rivin, E.I., 1983. Properties and prospective applications of ultra thin layered rubber–metal laminates for limited travel bearings. Tribol. Int. 16, 17–25.

Rosen, B.W., 1965. Mechanics of composite strengthening, Composite Materials. American Society of Metals, Metals Park, OH, pp. 37–75.

Schuerch, H., 1966. Prediction of compressive strength in uniaxial boron fiber–metal matrix composite materials. AIAA J. 4, 102–106.

Stören, S., Rice, J.R., 1975. Localized necking in thin sheets. J. Mech. Phys. Solids 23, 421–441.

Triantafyllidis, N., Bardenhagen, S., 1996. The influence of scale size on the stability of periodic solids and the role of associated higher order gradient continuum models. J. Mech. Phys. Solids 44, 1891–1928.

Triantafyllidis, N., Maker, B.N., 1985. On the comparison between microscopic and macroscopic instability mechanisms in a class of fiber-reinforced composites. J. Appl. Mech. 52, 794–800.

Triantafyllidis, N., Schraad, M.W., 1998. Onset of failure in aluminum honeycombs under general in-plane loading. J. Mech. Phys. Solids 46, 1089–1124.

Vogler, T.J., Hsu, S.-Y., Kyriakides, S., 2000. Composite failure under combined compression and shear. Int. J. Solids Struct. 37, 1765–1791.